UNIVERSITY OF CALIFORNIA, SAN DIEGO

FEASIBILITY OF USING NANOPOROUS MATERIALS IN WATER HARVESTING

A thesis submitted in partial satisfaction of the requirements for the degree Master of Science

in

Structural Engineering

by

Brian Justin Chow

Committee in Charge:

Professor Yu Qiao, Chair
Professor David Benson
Professor Qiang Zhu

2010

The Thesis of Brian Justin Chow is approved and it is acceptable in quality and form for publication on microfilm and electronically:

Chair

University of California, San Diego

2010

TABLE OF CONTENTS

LIST OF ABBREVIATIONS

AB50	acetylene black 50%
Al	aluminum
Au	gold
BET	Brunauer-Emmett-Teller
BP2000	Black Pearls 2000
C	coulomb(s)
C1	trichlorosilane
C8	octatrichlorosilane
C18	octadecyltrichorosilane
Cl	chlorine
cm	centimeter(s)
CNT	carbon nanotube
Cs	cesium
DI	deionized
E	exponent (base ten)
g	gram(s)
HMS	highly mesoporous silica
K	potassium, also Kelvin
kg	kilogram(s)
kN	kilonewton(s)
L	liter(s)
μm	micrometer(s)
M	molar (concentration)
m	meter(s)
min	minute(s)

mL	milliliter(s)
mm	millimeter(s)
mmHg	millimeter(s) of mercury
mol	moles
MPa	megapascal(s)
N	Newton(s)
Na	sodium
nm	nanometer(s)
PPI	pores per inch
PVDF	polyvinylidene flouride
s	second(s)
SS	stainless steel
UNF	Unified National Fine (thread)
V	volt(s)
W	watt(s)
ZSM-5	zeolite, Socony Mobil Number 5
ZY	zeolite Y

LIST OF FIGURES

LIST OF TABLES

LIST OF GRAPHS

ABSTRACT OF THE THESIS

FEASIBILITY OF USING NANOPOROUS MATERIALS IN WATER HARVESTING

by

Brian Justin Chow

Master of Science in Structural Engineering

University of California, San Diego, 2010

Professor Yu Qiao, Chair

The study on using nanoporous materials for harvesting water from the environment is still in its early stage, involving multiple methodologies, materials, and levels of technology. Insight on several experimentally novel directions shed light on the challenges and prospects associated with atmospheric condensation behavior, pressurized filtration, and ion adsorption on various nanoporous materials. The condensation of water throughout the surface of a porous cylinder was found to be difficult to extract in large quantities. In pressurized filtration, zeolites exhibit ion exclusion effects. It is also found that nanoporous carbon discs have a relatively low capacity of adsorption which is one order of magnitude insufficient to achieve a detectable decrease in solution salinity.

I. INTRODUCTION TO NANOPOROUS MATERIALS

A. Background Information, History, and Characterization

Nanoporous materials represent a major field of research in the context of current efforts in nanoengineering. Nanoporous materials are usually defined as matter (usually a solid) featuring structurally intact open channels or spaces and characterized on length scales less than 1 μm [1]. This is consistent with the general definition of nanostructured materials, which are characterized on length scales less than 1 μm.

The phenomena associated with small length scales of nanoporous materials are still regarded as in the infancy of experimental and theoretical investigations. We assume that many of the theories that apply to macroscopically observed phenomena (i.e., diffusion and surface tension) still hold in some respects, with some notable exceptions which will be further detailed.

The main characteristic of interest in nanoporous materials is their extremely high specific surface area, in units of area divided by mass. The high surface area is, in turn, due to the presence of channels and convoluted surfaces throughout a nanoporous material. We can illustrate the concept using macroscopic analogues with the following figure:

Figure 1.1 – All three blocks pictured occupy the same volume. However, the middle features a hole, and the one on the right features a convoluted surface. This increases their surface areas while decreasing their mass at the same time, resulting in greater specific surface area.

Another possible route for nanoporous materials to develop extremely tiny particles, but this feature plays a relatively minor contribution to the great surface area seen in some types of nanoporous materials. Nevertheless, surface area-to-volume ratio is an important factor in determining the specific surface area of a nanoporous material.

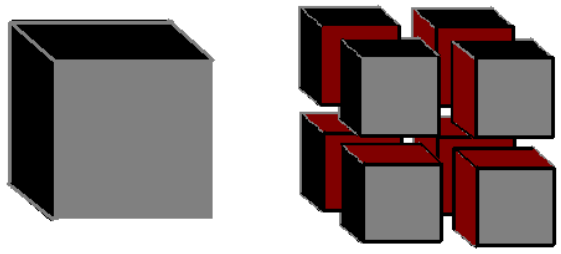

Figure 1.2 – An illustration of the surface area – volume ratio. The assembly on the right is cut across three mutually perpendicular planes. It has the same volume as the cube on the left, but has twice the surface area.

In Figure 1.2, we can see an example of the effect of splitting a particle, idealized as a cube, into smaller components. As the volume remains the same, the surface area increases. One can visualize that the model can be scaled all the way down into very small scales, until the scale of individual atoms is reached. When that happens, the split block on the right-hand side of Figure 1.2 represents the size of the atom clusters with new open faces. Because numbers themselves now trivially count the number of atoms on a side, and because the sizes of atoms always remain constant, the surface area – volume ratio on each individual block on the right-hand side is 2 times that of the single left-hand block.

Another important characteristic is the specific pore volume. The difference between Figure 1 and Figure 2 is that the former has a specific pore volume, but the latter does not, even though there are tree spaces among particles. In general the increase in surface area due to Figure 1.2 is not as great as that for Figure 1.1, in the context of nanoporous materials.

Many nanoporous materials have a morphology in which the interior spaces can be roughly simplified, for the sake of analysis, as a cylindrical hole. If the hole is smaller than 2 nm,

on the order of atoms and molecules, the material is defined as *microporous*; if between 2 nm to 50 nm, *mesoporous*; greater than 50 nm, *macroporous* [2,3].

Despite recent namesakes and technological intrigue, the history of peoples' uses of nanoporous materials stretches back thousands of years [4]. Arguably, a borderline nanoporous material is clay, with the characterization of it situated on the finer limits of conventional definitions of microscopic scales. Featuring particles on the order of 1 μm, the length scales of a minority of particles, and virtually all spaces between their gaps is actually in deficit of 1 μm. They were used for medicinal purposes (extracting toxins), bleaching textiles, and porcelain-making. Carbon black was also used in ancient times as a pigment.

In the 20th century, people have developed a variety of new nanoporous materials in addition to traditional clay powders, notwithstanding its newer uses as a moisture absorbent and deodorizer. Most of the development has been carried out over the last several decades, with specific focuses on tailoring nanoporous structure properties occurring as early as the 1970s [5]. During that time and the following decades, for example, carbon black, alumina, and silica materials were synthesized with specific surface areas greater than 100 m^2/g.

Development of nanoporous materials over the past century has been enormous, with some applications of nanoporous materials already used in everyday life. Silica gel is one of the most common examples, and their applications range from the packaging of goods to liquid chromatography. Invented in 1919, it was characterized by a high specific surface area of 500 m^2/g already by 1938 and, due to improvements in procedure, increased to more than 1000 m^2/g by the 1990s [7, 8].

Table 1.1 – A list of some physical properties of common nanoporous materials [5].

Some Physical Properties of Three Common Adsorbents

Adsorbent	Surface Area (sq. m/g)	Pore Volume (cc/g)	Pore Diameter (Å)
Activated Carbon	>1000	0.5-0.6	~20
Activated Alumina	~300	0.3-0.4	~50
Silica Gel	500-1000	0.4-0.5	~20

The characterization of nanoporous materials owes most of its technique to the theories and applications developed from the early part of the 20th century. The nature of gas adsorption using the kinetic theories of the gas-solid interface was developed by Irving Langmuir in 1916, although he was skeptical of any extension of plane-geometry adsorption techniques to measure nanoporous solids, which have complicated obstacles [9]. In 1938, another influential theory on gas adsorption, extended to porous analysis, was set forth by Brunauer *et al.* [10]. Known as BET theory, it gives the expression for specific surface area

$$S = \frac{N_A A V_M}{M_V W} \qquad (1.1)$$

where N_A is Avogadro's number (6.022 E23 molecules per mole), A is the area occupied by one molecule of an adsorbate, V_M is the volume of gas adsorbed at monomolecular condition, M_V is volume of one mole of adsorbate, and W is the weight of the sample. Usually, the adsorbed gas is diatomic nitrogen gas. BET remains one of the most-widely used methods for the characterization of pore specific surface area and specific volume. It is, however, still a simplification of the daunting task highlighted by Irving.

The surface properties of nanoporous materials are altered by special treatments on the surface. This can alter their interactions with liquids, as predicted from macroscopic observations. As mentioned above, surface treatments were mainly developed in the last few decades. Most of the surface treatments are made in order to study the effects of nanoporous materials with water, as it is the most abundant and essential liquid for living things.

B. Motivation for Research: Potential Applications

Research in nanoporous materials is continuously expanding as new and creative uses are being developed for their wide range of properties.

Intense efforts are underway to utilize the energy absorption of solid particles by a phenomenon related to a shear-thickening effect. Fluid mechanics explicates the shear stress of a fluid as

$$\tau = \mu \frac{d\theta}{dt} \qquad (1.2)$$

where τ is the shear stress and μ is the massed viscosity of the fluid, and $\frac{d\theta}{dt}$ is the rate of shear strain of an element of fluid. On a graph of τ versus $\frac{d\theta}{dt}$, one can see that normal liquids follow a monotonic linear relationship starting at the origin. If the curve is concave up, however, it is a dilatant, or shear-thickening, fluid [11]. It is known that aqueous suspensions of microscopic particles, which do not have particularly high specific surface areas (such as corn starch), are already subject to this behavior. The physical explanation may be related to the pressure-induced agglomeration of such particles under a high strain rate. Suspended nanoparticles may perform in a superior fashion due to an extra degree of freedom of liquid motion inside the particulate bodies. Combining with the techniques of surface treatment, the loading process can be developed to be reversible in nature. Ultimately, tthis has interest in “liquid protection” type technologies for helmets or vests.

Another area of interest includes the direct conversion of work done on nanoporous powder suspensions with a direct mechanical-to-electrical conversion scheme. The successful implementation of such a system would have enormous impact on green energy technology and render certain types of energy generation, *i.e.*, ocean waves, much more attractive. Yet another

conversion scheme is thermal to electric. This is based upon the capacitive effect, which characterizes electric potential developed between two nanoporous cells at different temperatures.

It must be stressed that at near-atomic scales many assumptions extending from the realm of classical (engineering) mechanics are made. In the atomic scales, however, quantum-mechanical effects are known to govern. For example, atoms cannot spin by themselves, but diatomic and larger molecules can, and only in discrete multiples of DOFs. Another example phenomenon between the classical and quantum world is the Debye length [13]

$$\lambda_D = \sqrt{\frac{\epsilon_0 \epsilon_r k_B T}{2 N_A e^2 I}} \qquad (1.3)$$

where λ_D is the Debye length, ϵ_0 is the absolute permittivity of free space, ϵ_r is the relative permittivity, k_B is Boltzmann's constant, T is the absolute temperature, N_A is Avogadro's number, e is the elementary charge, and I is a proportionality variable determined by the constituents of the surrounding environment, such as salt concentration. The Debye length is relevant in the analysis and understanding of nanoporous materials.

We can see that nanoporous materials are already useful for a variety of mechanical and electrical uses. In this thesis, we will focus our attention on the role nanoporous materials can potentially play in the harvesting of pure water from a variety of natural sources. Alternatively, their role in incrementally assisting in the desalination of water is investigated. First, an experiment involving air condensation using porous metals is carried out. Then, desalination is investigated with the properties of various nanoporous materials.

C. Main Categories and Routes of Synthesis

i. Carbon-based Nanoporous Materials

Carbon has many different allotropes. It was assumed in early times that there were two main allotropes of carbon. One was graphite, which consists of hexagonal parallel sheets, known as graphene layers. The other was diamond, where carbon atoms are arranged in a spatial network of carbon tetrahedra.

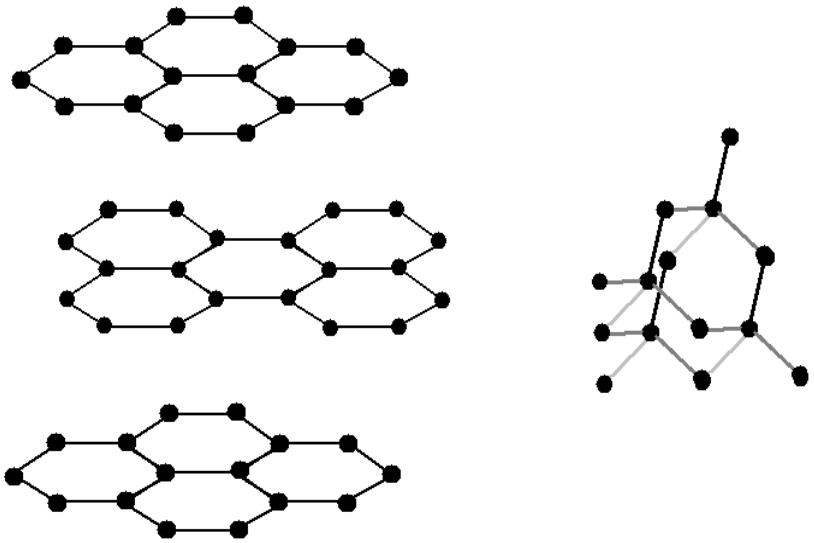

Figure 1.3- A schematic of the layers of graphite (left) and diamond (right).

Later it was known that far more carbon allotropes can exist. The discovery of the fullerene molecule was particularly a large motivation for further research on novel forms of carbon. Besides fullerenes, there are a variety of forms carbon can take. In the fiber form, it can be in carbon fibers, graphite fibers, or carbon nanotubes. The powder forms, such as activated carbon, features structures similar to graphite, but in an expanded and disordered form.

Generally speaking, the forms of carbon are produced from organic molecules using some form of high temperature, from flame pyrolysis to plasma temperatures. In the context of nanoporous solids, the important types include carbon nanotubes, carbon black, and aerogels.

The robustly inert nature of carbon under electrolyte solutions, as well as its ability to be organically modified at the surface underscores its importance for water extraction.

1. Carbon Nanotubes

A highly popular form of carbon in technical and popular literature is the nanotube. Originally, they were the by-products of C60 fullerene ("buckyball") synthesis. Sometime after the structure of the first nanotubes was first announced by Iijima in 1991, multiple procedures were developed for the synthesis of carbon nanotubes [14]. In 1995, single-walled nanotubes could be efficiently isolated.

Iijima's original method, and a method which is still commonly used for the production of CNTs, is the arc-vaporization method. This utilizes two carbon electrodes. The carbon electrodes could either be pure, or doped with a small amount of catalyst metal like iron, nickel, or cobalt [14,15]. Under a helium atmosphere of 500 mmHg, a DC current of 50-100 Amperes and potential difference of 20 V is applied, causing arcs to form across the chamber. A soot-like growth occurs on both electrodes at a rate of several millimeters per minute. Carbon nanotubes can then be extracted, amongst a host of other substances, from the soot. Usually, multi-walled nanotubes form more easily under such configuration.

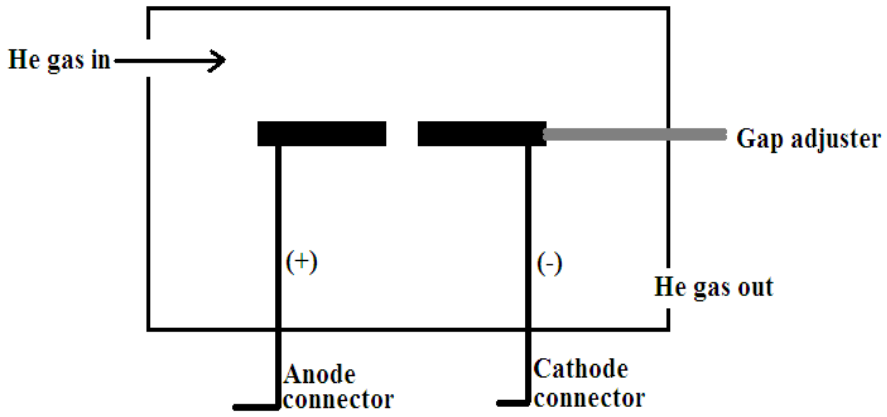

Figure 1.4 – A schematic for the production of carbon nanotubes. Coolant systems for the electrodes were omitted.

An alternative method to produce nanotubes is laser vaporization. A research group from Rice University developed a satisfactory method for continuous production of CNTs in the single-walled form. An inert atmosphere is heated to 1200 degree Celsius and 500 torr. A Nd:YAG laser (Neodymium yttrium aluminum garnet) laser impinges a graphite target composed of a small amount of catalyst metal, usually 0.5 to 1% Ni. A water-cooled copper collector positioned on the other end gathers the soot produced, and it is found to have CNTs of the single-walled variety.

2. Nanoporous Carbons

In this discussion, nanoporous carbons are divided into the groups of carbon black and carbon aerogels.

Carbon black is a powdered form of carbon that can be produced in industrial quantities from petroleum feedstock. The most often-used precursor is natural gas. For other types of carbon black, one can use a feedstock of oil, acetylene, or aromatic derivatives such as naphthalene [17]. Most production for carbon black is used as a filler and reinforcement for vulcanized rubber, but uses are extremely wide in scope. They are shipped in the free powder, but compacted forms are occasionally available.

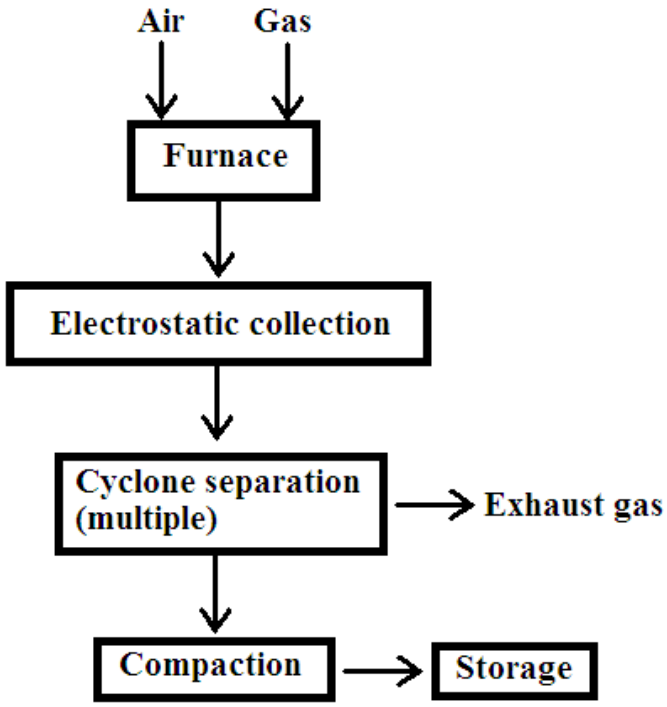

Figure 1.5 – A flow chart of the industrial process for producing carbon black.

Some processes of carbon black can achieve specific surface areas greater than 1000 m^2/g. In the research contained herein, the type of carbon that is of great interest is BP 2000, a furnace-derived carbon black. BP 2000 is conductive and has a specific surface area of roughly 1500 m^2/g [18].

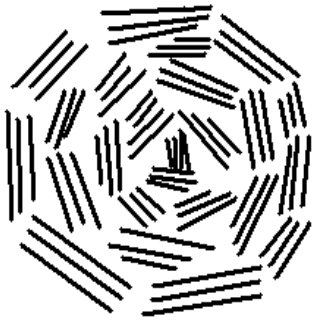

Figure 1.6 – A sketch depicting the simplified model of carbon black based on concept by Heckman and Harling [19]. Under oxidation, the radially positioned layers exfoliate.

The structure of carbon black greatly varies, because many rudimentary varieties only have a surface area of 100 m^2/g. Thus, it is expected that not all types of carbon black would

represent the same morphology on the nanometer scales. An obvious parameter influencing the behavior and performance of carbon black is the size of the particle. Size can be controlled by varying the temperature of combustion or decomposition of the feedstock hydrocarbon, as well as the amount of abrasion applied to the particles. Inside each particle, there are individual clusters held together by weak several layers of graphene sheets, separated by about 0.3-0.4 nm in distance. At the surface of each particle, the individual graphene sheets are perpendicular to the normal face.

Another major category of nanoporous carbon is its aerogel. Carbon aerogels are highly-networked and highly conductive forms of carbon black. They are generally formed by a polymeric network solid that is pyrolyzed at combustion-range temperatures [20]. The polymeric network solid can be polyacrylonitrile, phenolic resin, or polyurethane.

In order to fabricate a carbon aerogel, the polymeric network solid must generally also be an aerogel form. This is prepared using a gel curing technique.

An example is the resorcinol formaldehyde system in water. A catalyst (sodium carbonate) is added, and the water is replaced by acetone and then liquid carbon dioxide as the pore occupant. After slow out-gassing of the carbon dioxide, the polymer aerogel is then pyrolyzed, with accompanying volume shrinkage and mass loss. A nanostructured carbon, with the morphology of fused particles about 10 nm in diameter, is left after the pyrolysis is completed. The resulting material features a small pore size of 50 nm, a ‘string of pearls’ morphology, and high specific surface areas of up to 800 m^2/g. Their density can range from 0.04 to 1.3 g/cm^3.

Figure 1.7 – Carbon aerogel sample. The fragile nature is evident by the tear in the upper left corner.

ii. Silicate-Based Nanoporous Materials

Silicate-based materials investigated include mesoporous silica, which is a form of silicon dioxide with pores throughout small, spherical particles, and zeolites, which represent a class of silicate materials with occasional inclusion of elements other than the constituents of pure silica. Silica is generally an insulator, and as such, cannot be used for applications requiring electrical conductivity. However, because silicate-based materials are more chemically reactive than carbon, it is readily possible to attach a variety of organic or silicon-backbone molecules to the surface and dramatically change its electrostatic and polar interactions with other media, including fluids.

Figure 1.8 – Silica gel is an example of a commonly utilized form of mesoporous silica.

1. Highly-Mesoporous Silica

The form of silica known as highly-mesoporous silica (HMS) is made mostly through a chemical procedure involving organic silicate precursors mixed with several different surfactants. The surfactants serve to offer as an organic template for the silicate precursor, as a liquid "cast." It is also possible to replace the surfactant with a block polymer [20]. Some of the most widely-used silicate precursors are the organic silanes and orthosilicates, *e.g.*, tetramethyl orthosilicate [21]. Generally the technique is loosely grouped with the so-called nanocasting methods for other types of nanoporous materials (such as carbon), but is not truly classified as such due to the liquid nature of the surfactants. When mixed in an aqueous solution, the silicate groups in the precursors crosslink and solidify at room temperature. The organic remnants are then calcined at an elevated temperature, yielding the silicate structure [22].

It is also possible to obtain mesoporous silica through the acid leaching of certain types of glass. Currently, it is possible to use these methods to produce macroporous silicas [23]. A sample of glass is prepared in an inert crucible, using a comparable amount of alkaline oxides

compared to soda-lime glass. After the glass is made, a slow heat treatment of the glass forces a precipitation of soluble phases, and the glass is ground into a fine powder. When a solution of acid is added, the soluble phases dissolve, revealing the internal mesopores of the silica.

Silica surface treatments are available in a variety of ways. Among them include the C1, C8, and C18 reagents which serve graft onto the surface of the silica in the presence of nonpolar solvents at elevated temperatures. Newer developments make it possible to fabricate and surface treat HMS simultaneously [24].

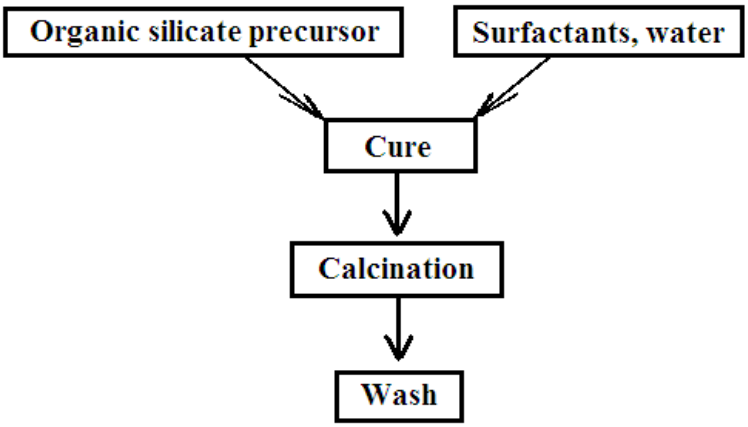

Figure 1.9 – A simplified schematic of the laboratory process for HMS synthesis.

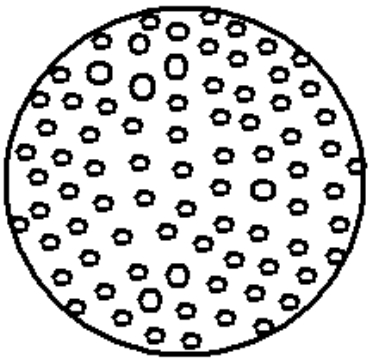

Figure 1.10 – A simplified schematic of an HMS particle with 'golf ball' morphology. Other forms exist.

There is at least one example where HMS can be generated from industrial waste. Agricultural sectors generate hexafluorosilicic acid from phosphate fertilizer production, which can be converted to HMS and other useful by-products [26]. Other methods include the use of liquid-crystal templates [27].

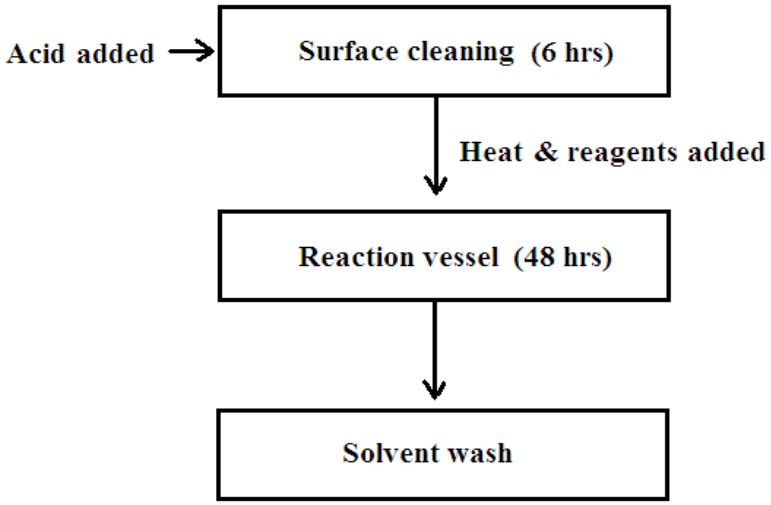

Figure 1.11 – A schematic of a surface treatment procedure for HMS.

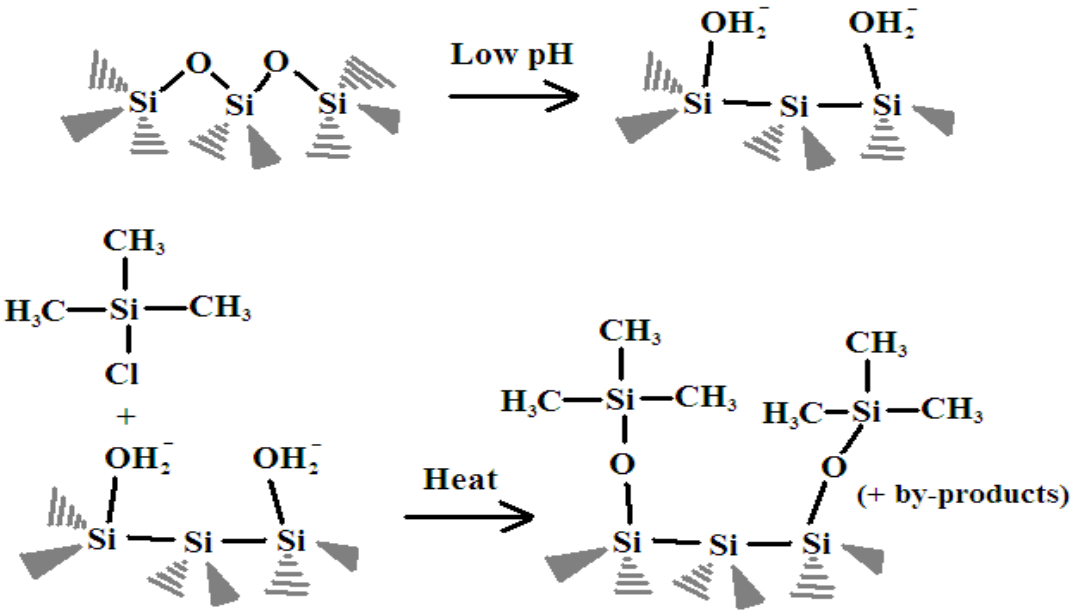

Figure 1.12 – A schematic of the chemical reactions involved in the surface treatment of HMS. (Courtesy Taewan Kim).

2. Zeolites

Zeolites are three-dimensional networks of crystalline or semi-crystalline silica and alumina, with alkaline earth cations present. Zeolites are naturally-occuring minerals in the earth's crust, by geochemical reactions between volcanic substrates and saline water. They were recognized for their behavior in acting as molecular filters, and as early as 1940 people had proposed methods in attempts to replicate natural zeolites in the laboratory, under different pH conditions.

Zeolites are generally synthesized from nucleation of a solution gel, using a molecular (cation) template such as tetrapropyl ammonium or sodium hydroxide [28]. Solutions of alumina and silica are added to supersaturate the aqueous solution or gel, which is then heated. The resulting solid is washed, heated, and separated out from organic precursors. Zeolites can be manufactured with different properties depending on the cationic templates present in the solution, the dilution of the solution, the silica to alumina ratio, the original form of the silica precursor, or the pH of the solution [29]. A zeolite that is extensively used in research and industry is the ZSM-5 variety, discovered in 1972.

Although the schematic depicted in Figure 1.13 appears to involve a greater number of procedural steps in the manufacture of zeolites, the overall cost of the zeolites in relation to highly mesoporous silica is relatively low. One reason for this is because the demand for zeolites is substantially greater than that of HMS.

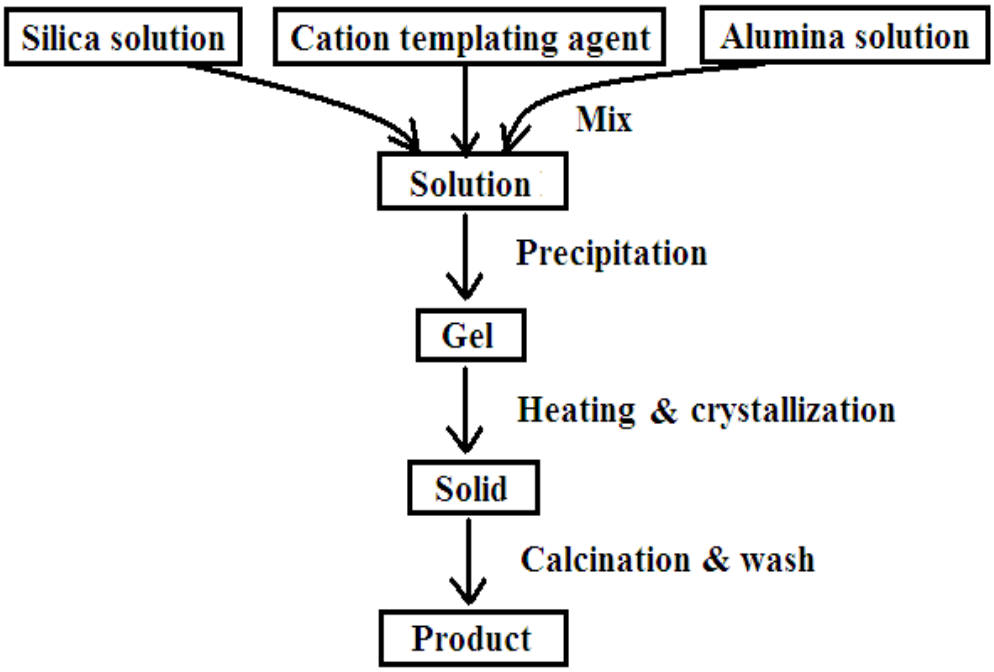

Figure 1.13 – A simplified schematic of the process in the manufacture of zeolites.

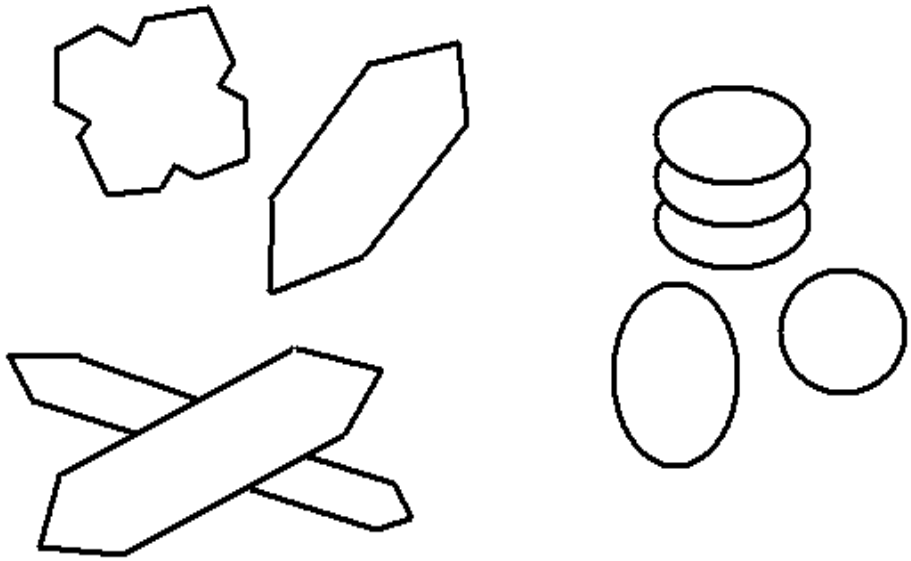

Figure 1.14 – A simplified sketch of crystalline particle morphology encountered for ZSM-5 type zeolite.

D. Possible Role in Water Harvesting

Carbon-based nanoporous materials are of interest for the desalination of water because they offer the advantages of ion selectivity and electrical conductivity. Ion selection has been demonstrated in the work of Fornasiero et al [13]. Conductivity plays an important role in in-situ electrolyte segregation under an induced potential difference; if the saline concentrations are detectable, the process can be iterated repeatedly until an acceptable minimum electrolyte concentration is reached.

In the work of Fornasiero et al, carbon nanotubes were modified by opening the endcaps of the tubular CNT structure and replaced by functional anionic groups. The functional groups included hydroxyl, carbonyl, and carboxyl groups. The CNTs featured pores less than 2 nm in diameter, effectively making it microporous. Electrolyte solutions, e.g. potassium chloride, were filtered through a CNT-containing membrane at 0.69 atmospheres, with the orientations of CNTS parallel to the direction of flow. An exclusion rate of 45% of chloride ions and 37% of potassium ions was reported. The mechanism of exclusion was determined to be electrostatic in nature, with electrostatic screening occuring near the functional groups.

The work with carbon nanotubes on water filtration is promising, for a number of reasons. First, it is possible to create functionalized CNTs through ionization and exposure to air [30]. Second, the oxidation-formed functional groups are robust in saline solutions. Third, electrolyte solutions pass through about 10 times faster than conventional nanopore membranes.

Carbon black, in the form of activated carbon, can be used for the filtration of water. This is possible by the specific adsorption of organic molecules (which is naturally a function of the specific area), and the compatibility and inertness of carbon in water. The process is generally observed to be effective, and used in ordinary household filtration products. A drawback is the finite lifetime of the carbon granules. The main difficulty with maintaining the full surface area of the carbon is the presence of natural organic matter in municipal water sources, even after steric filtration [31].

However, its ability of finer nanoporous carbon to segregate ions from a purely saline environment, such as seawater, less brackish water, remains relatively limited. The segregation of ions is almost exclusively electrical, with the requirement that conductive forms of carbon black (such as BP 2000) are arranged as electrodes. This is similar in fashion to the arrangement of a supercapacitor. If the pore volume is small enough, the ions will adsorb onto the carbon in one or possibly more layers, and there will be a detectable decrease in salinity. Furthermore, the process is reversible simply by switching the potential difference.

Carbon aerogels have also demonstrated potential as a desalinating agent. For this to occur, the setup is fashioned such that the aerogel is used as an electrode, and a voltage is maintained below the breakdown voltage of the electrolyte. Arrangement of the carbon aerogel electrodes, like carbon black, highly resembles that of a supercapacitor. The exceptions are that the salinity is monitored, and there is no need for a highly dielectric film. Using this concept, some significant results have been obtained [32,33].

Silicates are a frontier for a myriad of products, including water filtration. The surface properties of highly mesoporous silica can be modified to allow for attachment of functional organic groups. The significance of this is that it allows for the reversibility of pressure-induced infiltrations in HMS. A minority of the work done in the investigations herein involve using surface-modified HMS.

Zeolites offer uniformly microporous morphologies that allow water filtration from aqueous electrolytes. Because water forms complexes with the cations and anions of the solute, the effective size prohibits solute matter from entering the pore by purely mechanical means. Hydrophobic surface treatments can be performed for zeolite to facilitate an electrostatic exclusion. The behavior and salinity of electrolyte solutions outside of a zeolite are investigated in moderate scope.

Other nanoporous materials, besides the carbon-based and silicate-based ones, may have ability to isolate water related to high specific surface areas. The method is not necessarily filtration, but that of atmospheric condensation. As the atmosphere contains water, it is unknown

whether the high surface areas of materials may exhibit unusual phenomena apart from classical descriptions and observations of condensation. Apart from carbon and silicates, the material could be a nanoporous metal or ceramic.

The investigative portions of this thesis will consist of three experiments.

The first experiment will explore the role of water condensation on a macroscopically porous metal. The outcome of this experiment will determine whether or not further investigation is warranted for materials of the porous metal category, or altogether the fundamental strategy of water condensation from the atmosphere.

The second experiment will focus on the behavior of saline concentration in silicates, with the goal of the research aimed towards desalination of water. The outcome of this experiment will shed clues on the mechanism for ion exclusion from the various types of silicates, the overall efficacy of their role as a water filter, and the needed developments for realization of an effective water filter.

The third experiment will investigate the possibility of carbon electrodes on the in situ segregation of solute anions and cations in water, with implications for desalination. The outcome of this effort will determine whether the carbon widely produced today can be utilized for the cost-effective and high efficiency desalination of water.

II. EXPERIMENT: ATMOSPHERIC CONDENSATION ON POROUS SOLIDS

A. Motivation and Background

Air is normally composed of nitrogen, oxygen, water vapor, argon, and small quantities of trace gases. The water vapor is usually excluded from the compositional analysis of dry air, but nevertheless constitutes a sizeable portion of the earth's atmosphere somewhere between oxygen and argon in terms of mole fraction.

There are several ways to describe the concentration of atmospheric water vapor. Relative humidity describes the relative fraction of the concentration of water vapor to the saturated condition at the same temperature and pressure. For the purposes of water extraction from the atmosphere, this definition alone is not a complete description. The other needed definition is the absolute humidity, which specifies the concentration of water in terms of grams per cubic meter of air. The maximum absolute humidity (that is, at saturation) can be seen in Table 2.1.

Table 2.1 – The saturation (maximum) absolute humidity for atmospheric water vapor at different temperatures. The gray shaded area represents room temperature. (Adapted from [34].)

Absolute Humidity at Saturation for Different Temperatures

Temp. (°C)	Absolute Humidity (grams/m^3)
-10	2
0	5
10	10
20	18
25	23
30	32
35	40

Graph 2.1 – A representative trend of absolute humidity as a function of temperature. Both axes are linear (Adapted from [31].)

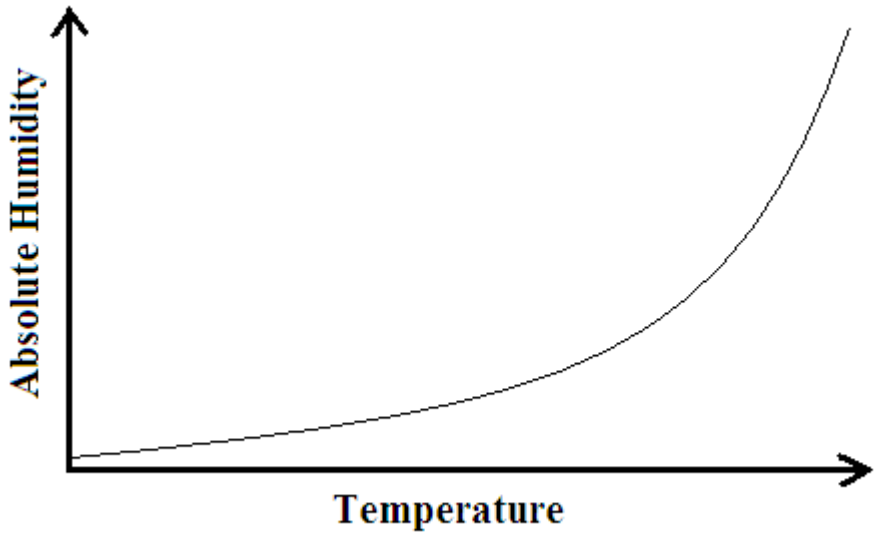

From Table 2.1, it is inferred that ordinary room temperature air can hold a maximum of 23 grams of water per cubic meter. Because that value represents a maximum, the actual value encountered in everyday situations is much lower than this. However, in Graph 2.1, a non-linear increase in the saturation water vapor is seen. Re-examining Table 2.1 leads to the conclusion that the nonlinear behavior is manifested around a value in the vicinity of, and above room temperature. The large difference in saturation pressure is responsible for the condensation between night time and day time temperatures, e.g., on blades of grass or car windshields. The critical assumption is that the particular absolute humidity level during the daytime temperature maximum is not close to zero; in other words, there cannot be a dry spell – otherwise, the dew point will occur at impractically low temperatures.

One can anticipate the quantity of water held by an ordinary room. For daytime maximum temperatures of 30 degrees Celsius, and a nighttime minimum temperature of 15 degrees, the difference in absolute humidity at saturation can be estimated (per Table 2.1) as 17

grams per cubic meter. If the room has a volume of 200 cubic meters, this can translate to 3.4 kilograms of water. Several liters of water can be extracted from the room in this circumstance, but the assumptions are optimistic. First, the air is saturated, and this is not necessarily the case in reality. Second, the temperature differences at saturation (occurring in the tropics and other humid climates) may not be as great as for arid regions of the world. A more realistic estimate is approximately 1 kg of water for the room if these factors are taken into account.

Nevertheless, the possibility of extracting water from a high surface area is open to investigation for its own reasons. Despite large volumes of air required, water vapor can diffuse freely in air until it contacts a surface as condensation, ideally requiring no work-derived energy for transport. In a material with extremely high specific surface area, the surrounding air could diffuse inside in order to deposit its water content, and then diffuse out. Small particles from condensation, as in a fog or mist, can similarly adsorb via the Brownian motion of the air. As long as the surface lining the inside pores of the solid are hydrophobic, the water can be continuously emptied out into a container from gravity, again using no work-derived energy. Over many hours, the diffusion process on a sizeable but portable piece of porous material may transport more water than the room in the above example. Assisted, slow flow rates of cold air through the porous solid can also improve the process, provided that condensation is not interrupted.

The condensation of water can occur on any surface, even on a hydrophobic surface-treated material. Both carbon and silica, in their bulk forms, are capable of a viable condensation substrate. However, because of large amounts of expense associated with producing larger samples, and due to the difficulty of utilizing them with large amounts of air flow, they are discouraged from the scope of the experiment.

B. Experimental

The surface of a macroscopic aluminum foam metal (Manufacturer: Duocel) with characteristic pore density of 40 PPI was subjected to surface treatment. Five samples were cut out, weighing 0.2 – 0.4 grams apiece. The samples were each immersed in a 5 wt% oxalic acid solution for 5 hours. The samples were then taken out to be washed and dried for 12 hours. In the second step, the samples were immersed in a solution containing 20% C1 reactant by volume, with the balance consisting of toluene solvent. After 5 minutes of immersion, the samples were heated to 80 degrees Celsius in a bicuspid valve flask with a condenser column. The solution containing the samples were agitated continuously using a magnetic stirrer. After 48 hours, the heat was turned off, and the samples were taken out for rinsing. The rinsing solution consisted of DI water, toluene, water again, and acetone, separately and in that order. The samples were dried for 48 hours at a temperature of 100 degrees Celsius. The process is repeated for C8 reactant to impart a greater degree of hydrophobicity.

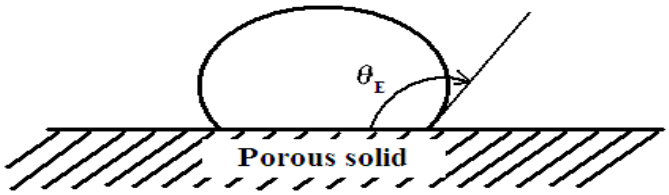

Figure 2.1 – A depiction of the wetting angle used to test for hydrophobicity after a surface treatment, as indicated by the obtuse angle drawn.

The surface treatment procedure was repeated for monel cylinders of dimensions 9.5 mm diameter by 19 mm height, with a pore size of 120 PPI.

The samples of hydrophobic aluminum were tested for hydrophobicity using one drop of DI water. A hydrophobic drop is depicted in Figure 2.1. The samples are then exposed to 0

degrees Celsius, -25 degrees Celsius, and -196 degrees Celsius (in liquid nitrogen) environments, each for five minutes. They were then taken out and exposed to a small jet of supersaturated moist air at 25 degrees Celsius moving at 1 m/s. The condensation was observed over a microscope and qualitatively examined.

The monel cylinders were installed inside of a tubing (Tygon) apparatus connected to a pump (Omega FPU-5MT). A 0.005-inch thick electrolytic-grade copper sheath was wrapped around the outside of the monel cylinder before insertion into the tube. An appendage of the copper sheath was connected to an exterior coil of an immersion chiller (Polyscience KR-50A) set to a temperature of -40 degrees Celsius. The connection was made using drops of DI water. The condensation at various flow rates for the pump was observed.

Figure 2.2 – Photo of porous aluminum samples which exhibited hydrophobicity after C8 surface treatment, with a penny shown for scale.

Figure 2.3 – Photo of the monel cylinder, surface treated with C8, with a penny shown for scale.

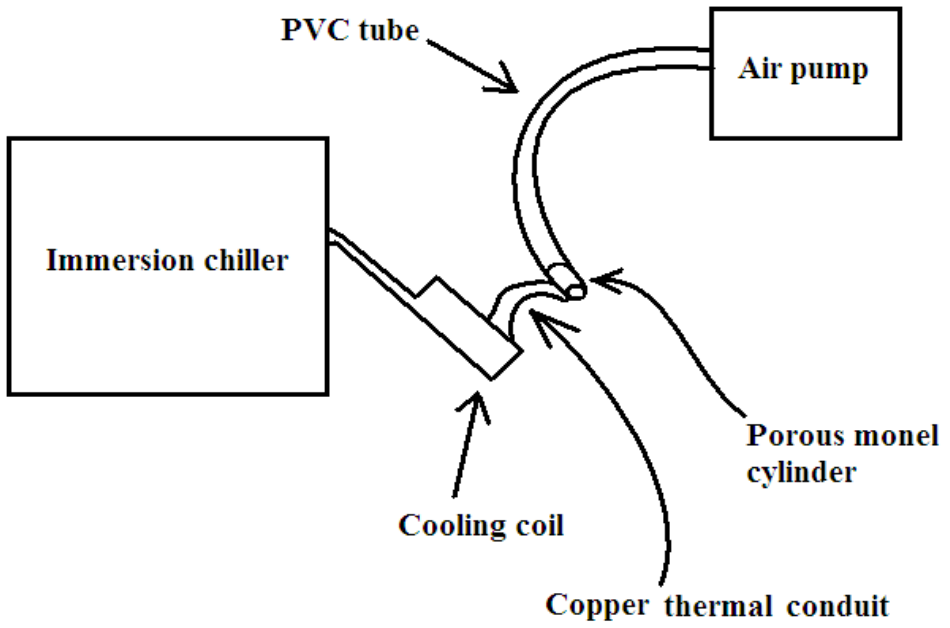

Figure 2.4 – A schematic of the setup of the condensation of water by forcing air through porous monel.

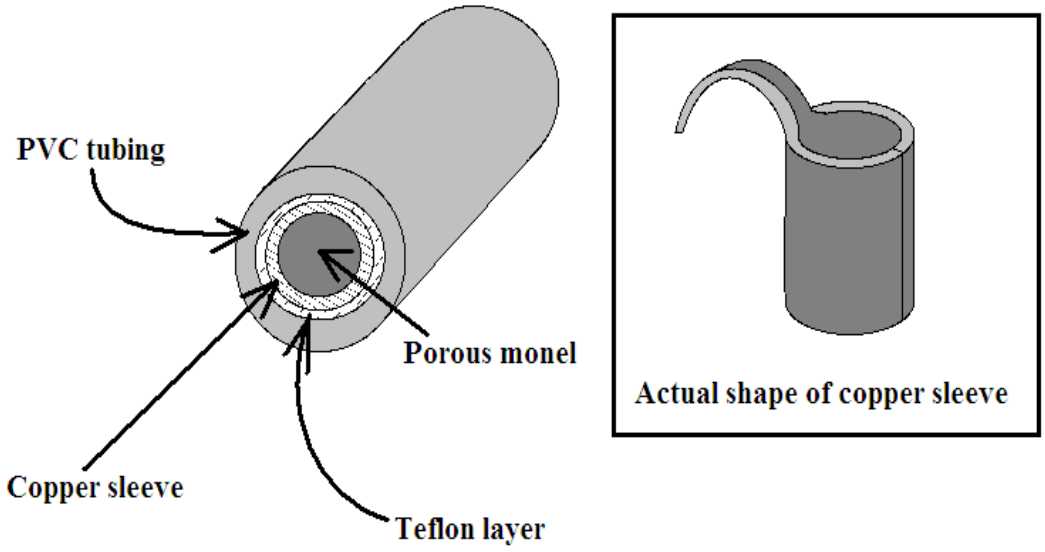

Figure 2.5 – A zoom of Figure 2.5, showing the detail of the monel cylinder at the end of the PVC tube. The insert depicts the thermal bridge of the copper sleeve, which extends out and connects to the chilling coil.

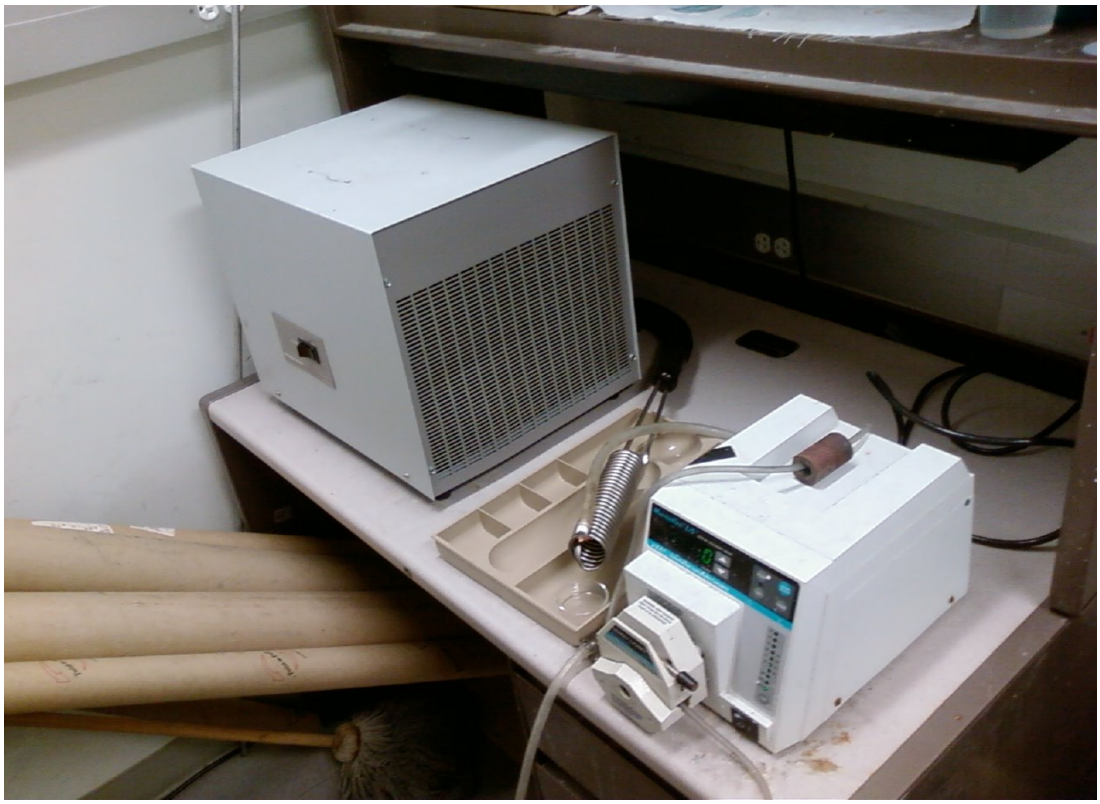

Figure 2.6 – A picture taken of the setup configuration of the immersion chiller, air pump, tube, and monel cylinder.

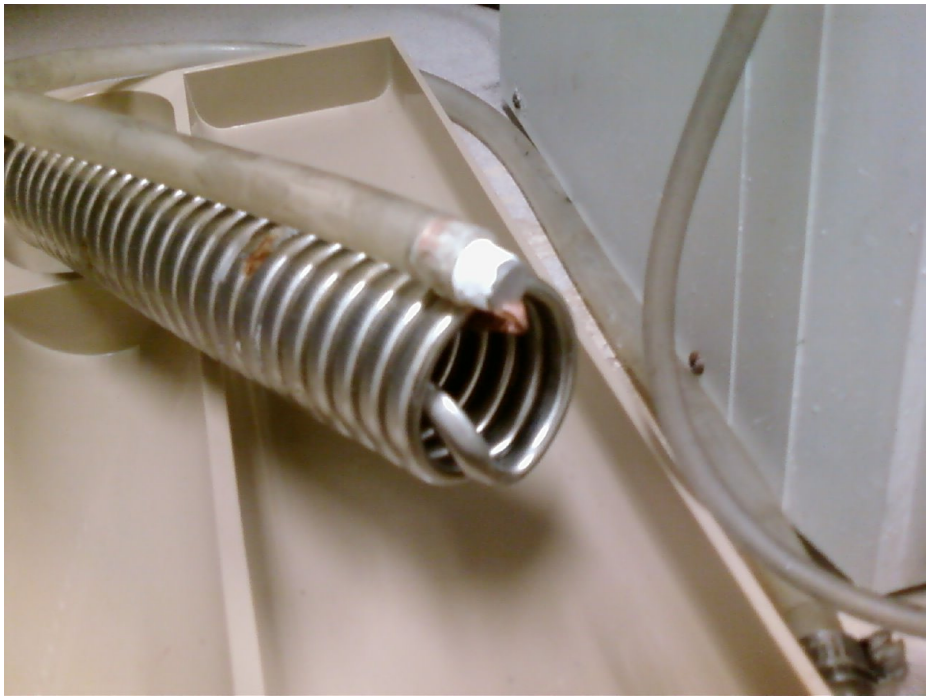

Figure 2.7 – A closeup of the chiller coil and the monel cylinder, attached by the copper sleeve.

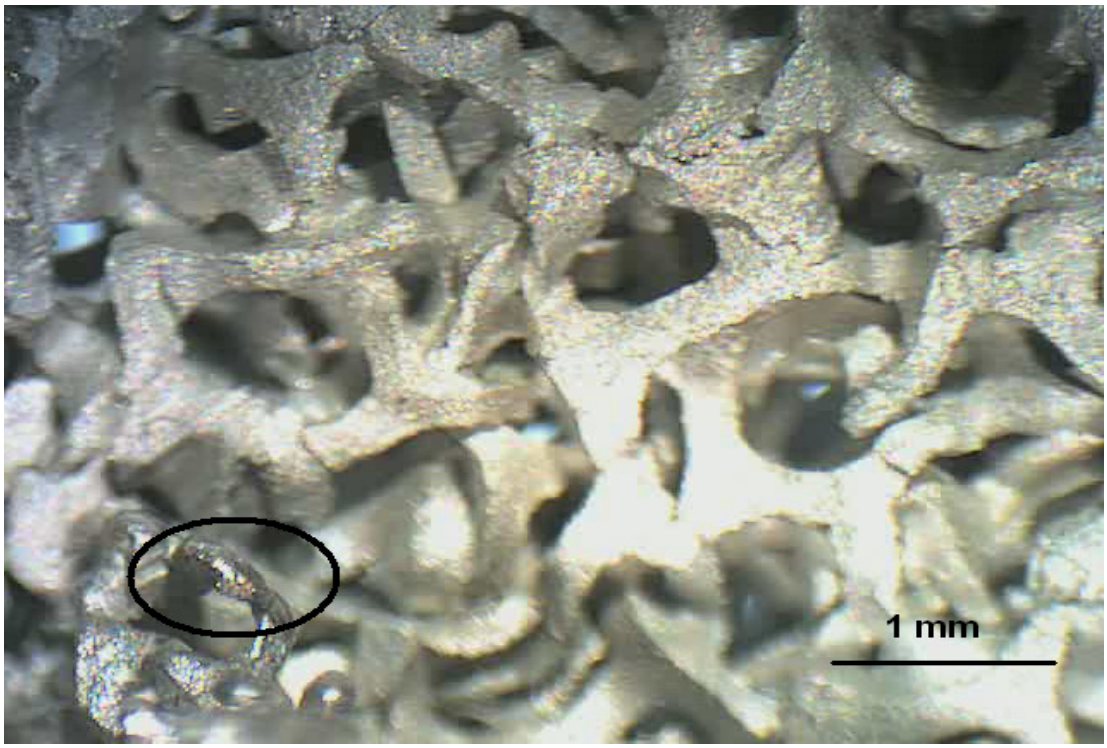

Figure 2.8 – A view of condensation formation on aluminum, in the early stages of condensation from a -10 degree Celsius environment, at magnification of 20X. A drop is shown in the black circle.

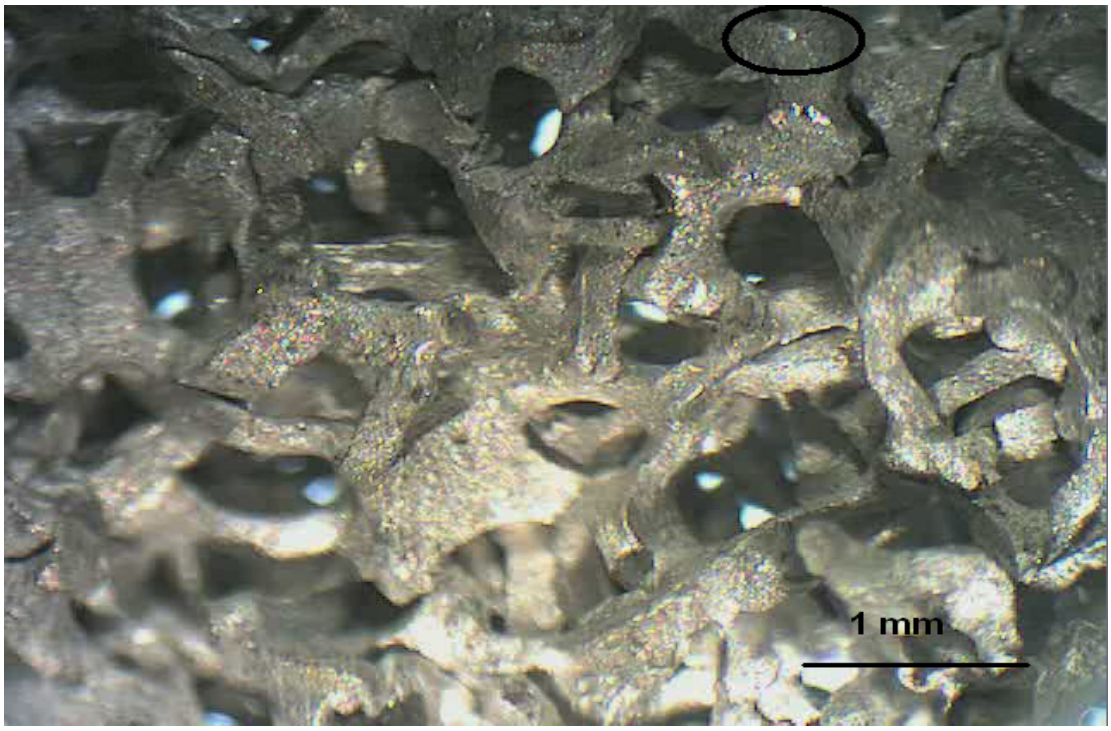

Figure 2.9 – A view of condensation formation on aluminum from a -10 degree Celsius environment, with a drop circled in black. Magnification is 20X.

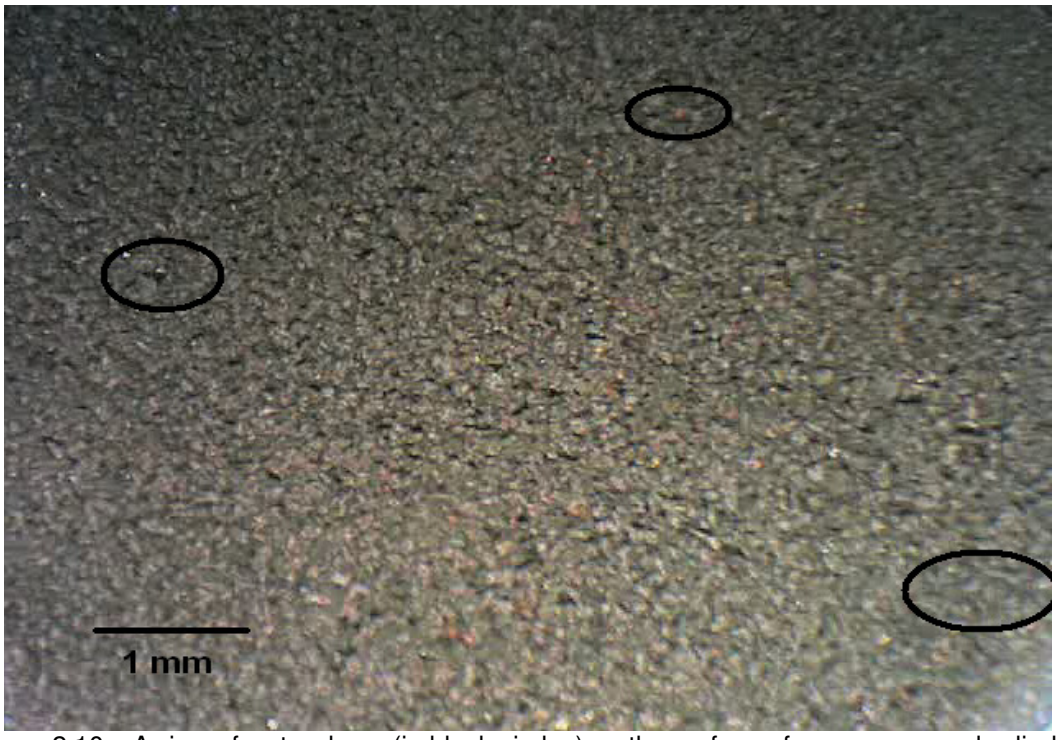

Figure 2.10 – A view of water drops (in black circles) on the surface of a porous monel cylinder, brought from a 0-degree environment. Magnification is 20X.

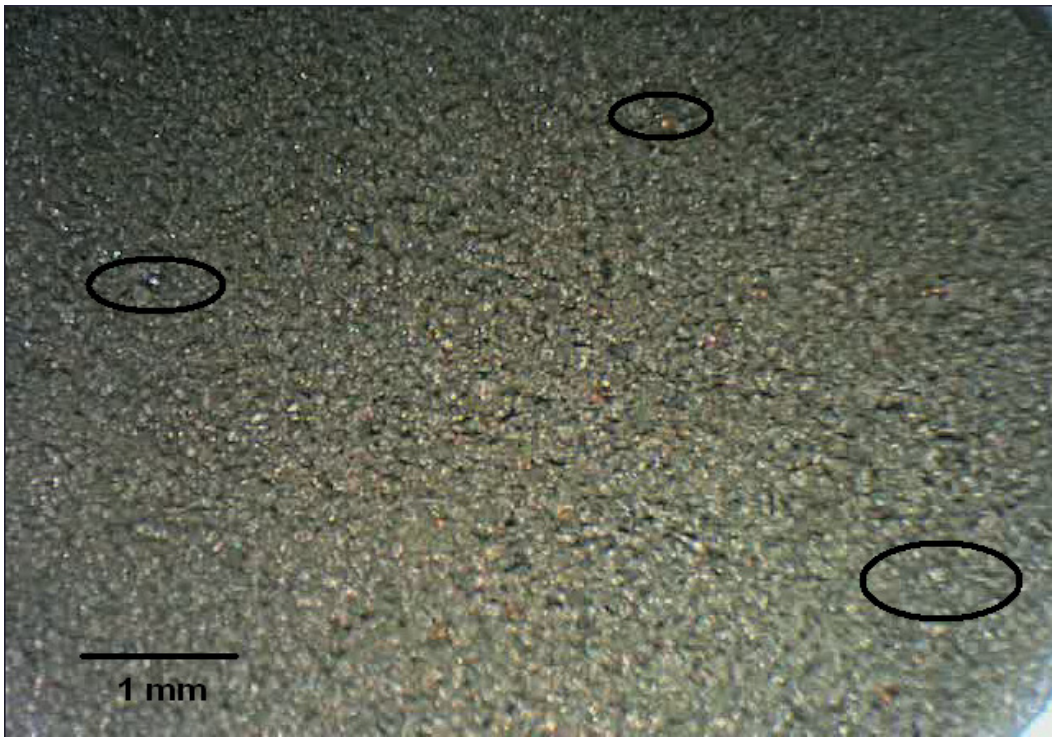

Figure 2.11 – A view of water drops, from the same area on the monel cylinder, taken 3 minutes after Figure 2.10. Magnification is 20X.

C. Results and Discussion

Upon the testing the degree of hydrophobicity of the surface-treated aluminum, one sample was found to absorb DI water and thus rejected from the experiment. The remaining four samples, which were treated with C8, showed hydrophobicity from an obtuse wetting angle.

The hydrophobic samples all showed no visible signs of surface moisture buildup when exposed to moist air from the 0-degree environment. At -20 C, however, they showed some evidence of water droplets, but the density of significant droplet formation was sparse under the magnified view of the microscope. The moisture collected for several minutes, and evaporated thereafter. When viewed after extraction from the -196 C environment, more condensation was observed in the form of ice crystals.

It is clear that the temperature influence on the quantity of condensate is relatively pronounced.

For the monel cylinder, the elapsed time for one drop to be extracted from the end of the apparatus was 5 hours.

Due to the configuration of the monel cylinders, it is difficult to extract conclusive evidence of a specific surface area link on the quantity of condensate. The main difficulty arises from the temperature profile inside of the monel cylinder, and the presence of air flow through the pores of the structure. The air flow replenishes heat taken out from the refrigeration unit, and thus renders an additional difficulty in determining whether the inside surfaces can be continuously cooled. The one-dimensional temperature distribution inside the monel cylinder which satisfies the heat equation [35]

$$\frac{d^2T}{dx^2} + \frac{\dot{q}}{k} = 0 \qquad (2.1)$$

is expressed in the form [35]

$$T(r) = T_s + \frac{q r_0^2}{4k\left(1 - \frac{r^2}{r_0^2}\right)} \qquad (2.2)$$

where $T(r)$ is the temperature distribution, T_s is the temperature of the copper sleeve, $\dot{q}$ is the energy replenished inside the monel cylinder per unit volume due to air flow, k is the thermal conductivity of the monel cylinder, r_0 is the radius of the cylinder, and r is the radial coordinate. The energy generation term can be calculated as

$$\dot{q} = \dot{V} \rho c_p \Delta T \qquad (2.3)$$

where $\dot{V}$ is the volume flow rate of air, ρ is the density of air, c_p is the specific heat at standard pressure of air, and ΔT is the temperature difference between the air and the chilled copper sleeve. Assuming that the thermal conductivity of the porous monel cylinder is 2 W/m K, the flow rate is 6 mL / min, the density of air is 1.3 kg/m^3, the specific heat of the air is 1.007 kJ/kg K, and the temperature difference is 25 degrees Celsius, a parabolic distribution between r=0 and r=r_0 is expected to develop. The rate term on the right-hand side of Equation (2.2) amounts to less than one tenth of a degree in change, which gives a constant profile. The calculation suggests the flow rate to have minimal impact on the radial temperature distribution of the monel cylinder.

Given that the temperature inside the monel cylinder is roughly uniform, there are other factors which must govern the performance of the system. One possibility is the formation of ice or pre-existing droplets from the condensation, which serves to impede the flow of both air and water. Because the temperature of the cooler device was constant, the setup could not be altered in a trivial way to permit dew-point temperatures from being reached throughout the porous monel cylinder. Adjusting for a faster air flow rate would favor the re-vaporization of condensate due to pressure decrease.

D. Conclusion and Prospectus

The air condensation on a porous solid represents a key interest in the field of water extraction and isolation from natural surroundings. Through a series of experiments, the difficulties facing the development of such a device mainly arise from the transport of air through convective processes, bulk flow (i.e., from wind), or molecular diffusion. The dew point is satisfied in the environment, but is exaggerated on the laboratory scale due to the small sample size of the porous solid. The use of two realistic refrigeration regimes, namely 0-degree and -20 degree Celsius environments, showed evidence of water droplet formation on a hydrophobic-treated metallic sample. The exaggerated temperature of -196 degrees Celsius was realized through the use of liquid nitrogen, and brought about substantial observed condensation, but in the immobilized form of ice.

The flow rates used in the apparatus containing the monel cylinder simulated a device utilizing high surface area with refrigeration and forced bulk flow combined. While it was found that the rate of water accumulation in the cylinder pores was limited, the reason for the observed decrease was due to a combination of freezing and evaporation due to the localized reduction of pressure of air inside the pores. As long as the flow rate is minimal, on the order of one ten-millionth of a liter per second, water drop formation will occur.

Small scale experiments show that the forced condensation of water on porous solids is difficult when air is forced upon a continuously-cooled sample, or when a non-continuously cooled sample is subjected to environments of saturated water vapor. Diffusive transport of water into large, porous solids with hydrophobic surfaces remains an open question.

III. EXPERIMENT: ION EXCLUSION OF SALINE SOLUTIONS WITH ZEOLITE

A. Motivation and Background

Water desalination represents a significant portion of efforts for the isolation of water from natural environments. The ultimate motivation behind a successful and economically viable desalination system is the virtually unlimited supply of fresh water from the world's oceans. In the introduction, a brief mention was made on the progress of novel types of membrane filtration systems based on end group-modified CNTs. While there is significant attention paid to the role of membrane filtration configurations with CNTs, the application of various nanoporous materials outside of the carbon-based materials is less known.

A preliminary assessment considers the formation of hydrated complexes in the solution across a semi-infinite solid surface, which forms a double layer, composed of Helmholtz and Stern planes [38]. The extension is of this scheme for mesopore sizes may be tentative, but for microporous materials the analogy is less appropriate. The former is characterized by an immobilized layer of adsorbed cation complexes, and the latter by semi-free moving complexes. The scale of the double-layer is characterized by the Debye length, which from [13] is estimated on the order of 1-10 nm. The Pauling sizes of the different cations available for disposal are given below.

Table 3.1 – Selected Pauling sizes for different cations (From [36].)

Cation	Pauling Size (nm)
Li^+	0.12
Na^+	0.18
K^+	0.26
Cs^+	0.34

In this experiment, we seek to determine if there is an ion exclusion effect of zeolites, when placed in various saline solutions under a monotonically increasing pressure. In particular,

the salinity dependence on the direct application of ZSM-5 and ZY under various pressure loadings is an open question, because it is difficult to measure instantaneous salinity at pressures higher than that occurring at or above infiltration. The expectation is that because the pores of zeolite are regarded as microporous (less than 2 nm), a salt solution should exhibit some type of pressure-induced exclusion outside of the zeolite surface.

If the process is purely steric, a threshold size of ion may be encountered by which larger ions in aqueous solution are always excluded from the zeolite pores. The significance of the outcome will determine whether it is worth to desalinate an electrolyte solution using zeolite powders or membranes.

B. Experimental

A load cell was utilized for the purpose of liquid confinement. The load cell (Figure 3.5) consisted of a thick annular cylinder with an inner circular hole of diameter 19 mm and area 284 mm^2. A piston of matching size was inserted into the load cell, with a rubber O-ring located 4 mm offset from the contact end. The material comprising the cylinder body and piston was 304 stainless steel. For extracting small amounts of liquid under pressure, a custom-made tap apparatus was utilized, also seen in Figure 3.5. The tap was machined from 316 stainless steel, with an outside tap of diameter of 1.19 mm (designation 0-80 UNF). Allen screws of matching diameter are fastened on the tap. The tap itself is fastened by parallel wrench-torqued surfaces and sealed with two consecutive o-rings, included in Figure 3.5.

Two types of zeolites, as well as a few HMS, are used in the course of the experiment. The two types of zeolite are ZY (Zeolyst CBV-901) and ZSM-5 (Zeolyst CBV-28014). The ZSM-5 is characterized by a silica-to-alumina ratio of 280:1. Characteristics of the zeolite were determined using nitrogen adsorption analysis, with BET analysis. The ZY has a specific surface area of 700 m^2/g, a specific pore volume of 240 mm^3/g, and an effective pore diameter of 0.6 nm [36]. The ZSM-5 has a specific surface area of 800 m^2/g, a specific pore volume of 220 mm^3/g, and an effective pore diameter of 0.7 nm [34]. The particle size for both zeolites is on the order of tens of μm. Both zeolites underwent a hydrophobic treatment procedure [36, 37]. Contaminant adsorbates on the zeolites were purged by heating in an open-air furnace at 550 degrees Celsius for 6 hours. The HMS samples have pore diameters of 6 nm and 10 nm, and surface treated with C1 and C8 respectively.

The tap apparatus was prepared according to Figure 3.4. A porous filter was manually packed to a high density inside the hole where the solution enters to filter the solution from the zeolite. Two o-rings were used to secure the tap to the load cell at the compressive face, in order to seal the liquid. Considerable torque was used to secure the tap securely to the load cell. The tap screw (0-80) was fully tightened on the outside tap face.

A refractometer (Westover Model RHS-28) was calibrated using DI water. Throughout the experiment, regular calibrations were performed using DI water to check the accuracy of the refractometer. If there is more than 0.2% difference from zero, the refractometer was re-calibrated.

Using an electronic balance, 2.27 grams of zeolite crystals were weighed out. Then, the refractometer was used to check the salinity of a stock salt solution, which is adjusted to standard initial salinity. Out of the stock solution, 5.2 mL were added into the load cell and stirred briefly. A refractometer was used to gauge the salinity of the solution again, in order to check contaminant solutes. The zeolite was then added into the salt solution inside the load cell, creating a suspension, and the cap was sealed. The salts tested were the chlorides of lithium, sodium, potassium, and cesium. In the case of HMS, 5.6 mL of a 15% sodium chloride solution was used. The solvent used was water in all cases.

The complete load cell was tested using a compression machine (Instron type 5582) with a constant loading rate of 5 mm/min. For ZSM-5, the maximum compression load was 90 kN; for ZY, on the order of 1 kN; for HMS, to 10 kN. The hydrostatic pressure may be calculated as the engineering stress

$$\sigma = \frac{F}{284\ mm^2} \qquad (3.1)$$

Where F is in Newtons and σ is in MPa. Once the peak load was reached, the machine paused and a few drops of saline solution were collected through the tap screw. Several readings were taken, with the mode value taken as the salinity anomaly.

To control against the presence of contaminant solutes inside the load cell, a 0.582M salt solution of sodium chloride was added without zeolite, all else remaining the same.

To control against possible evaporation during the experimental procedure, a 0.582M sodium chloride solution was added to the load cell, but no zeolite was added and the cap was left off, exposing the solution to the atmosphere for 15 minutes. A study on the rate of evaporation from a drop spread thinly over the refractometer surface was also done.

To control against the presence of contaminant solutes inside the zeolite, a 0.582M salt solution of sodium chloride was added to 2 grams of ZSM-5 in a vial. The suspension was sealed and agitated by shaking, then left to separate overnight. The salinity of the clear portion was then checked.

Figure 3.1 – A photo of a crucible containing ZY. Both ZSM-5 and ZY are fine white powders.

Figure 3.2 – A photo of the 10-nm C8-treated HMS, on the left, and the 6-nm C1-treated HMS, on the right. The left appears slightly brown due to oxide contamination after a test.

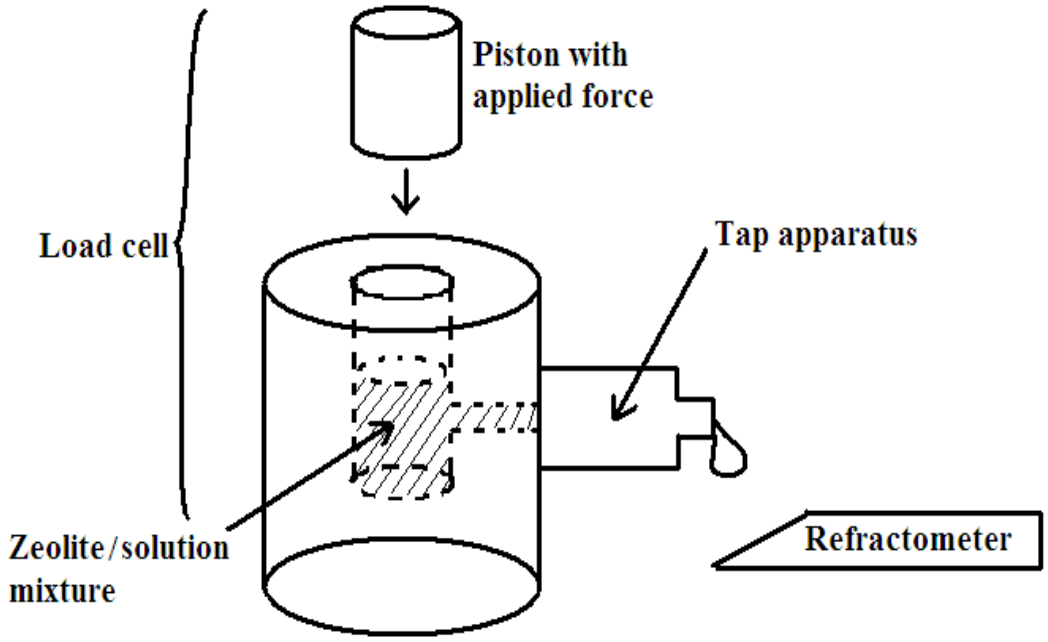

Figure 3.3 – An schematic of the experimental setup for compression testing.

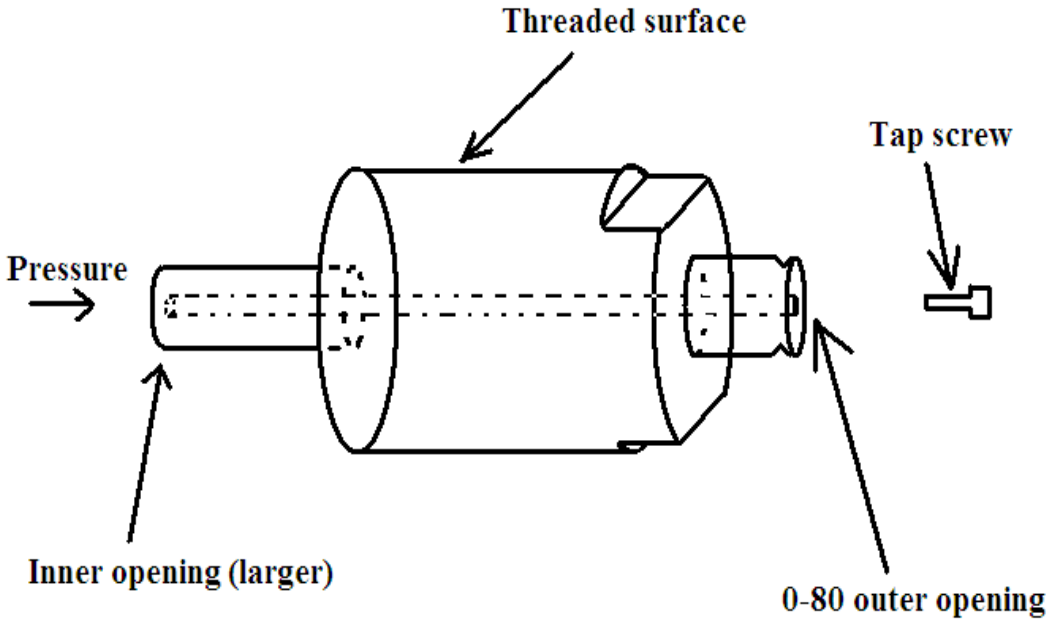

Figure 3.4 – An illustration of the complete tap apparatus.

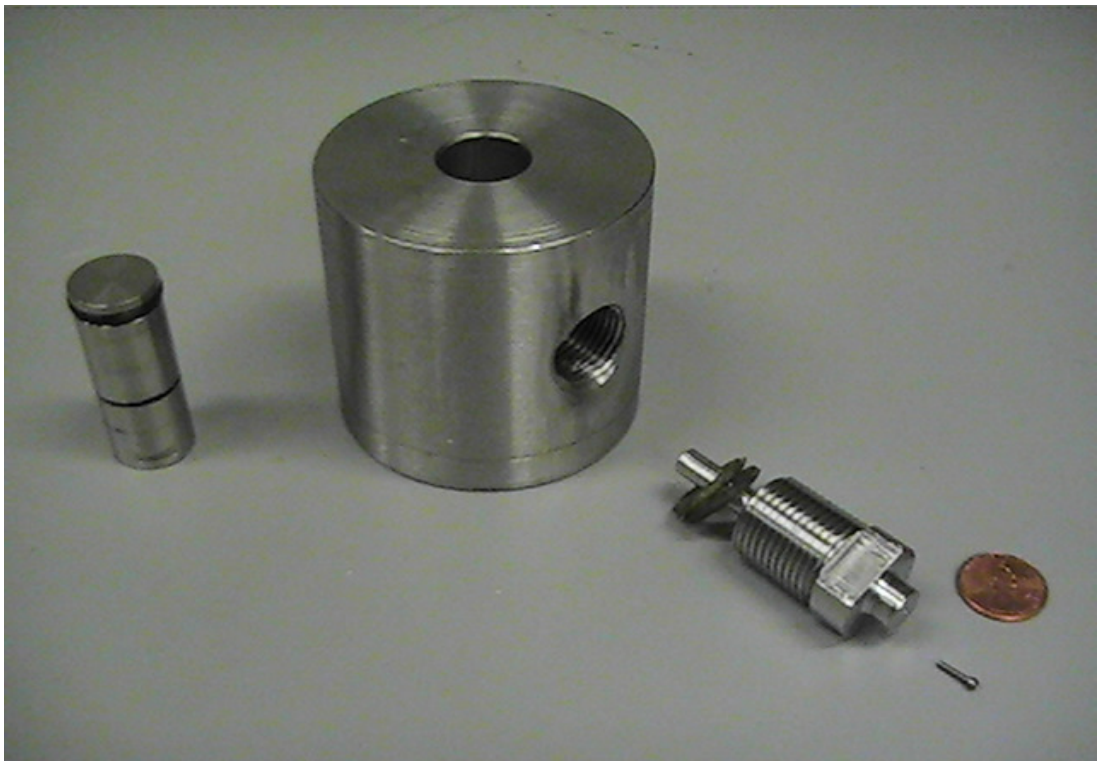

Figure 3.5 – A photo of the main components of the load cell before assembly. A penny is shown for size comparison.

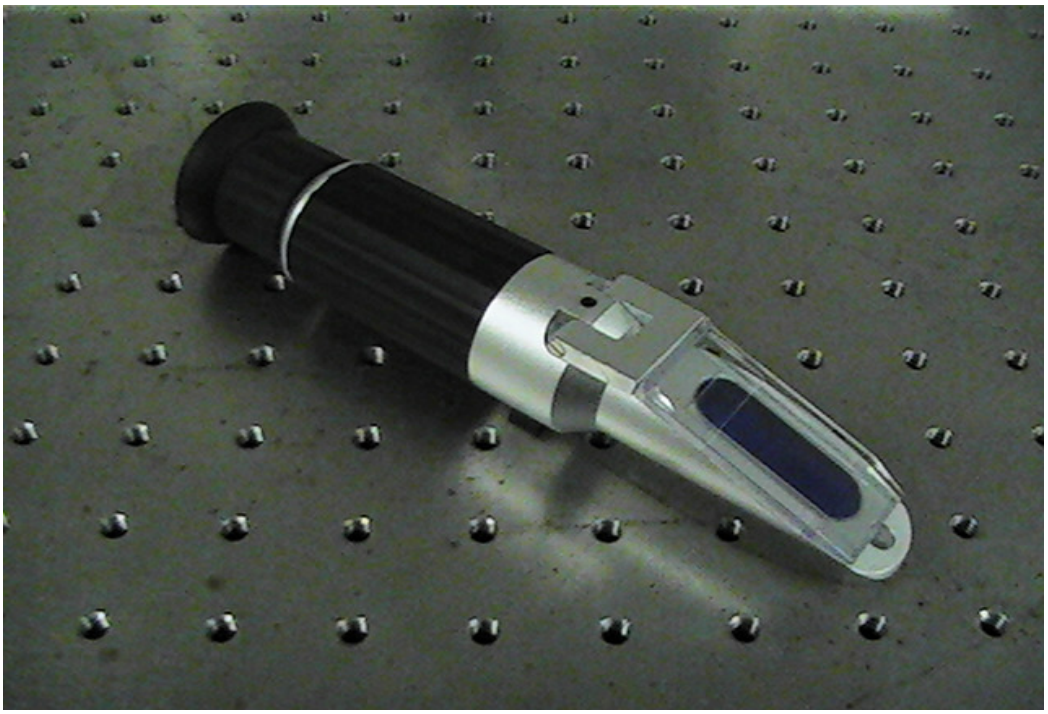

Figure 3.6 – A photo of the refractometer. The salt solutions were added to the slanted blue panel on the right. The eyepiece (not shown) is located on the left end.

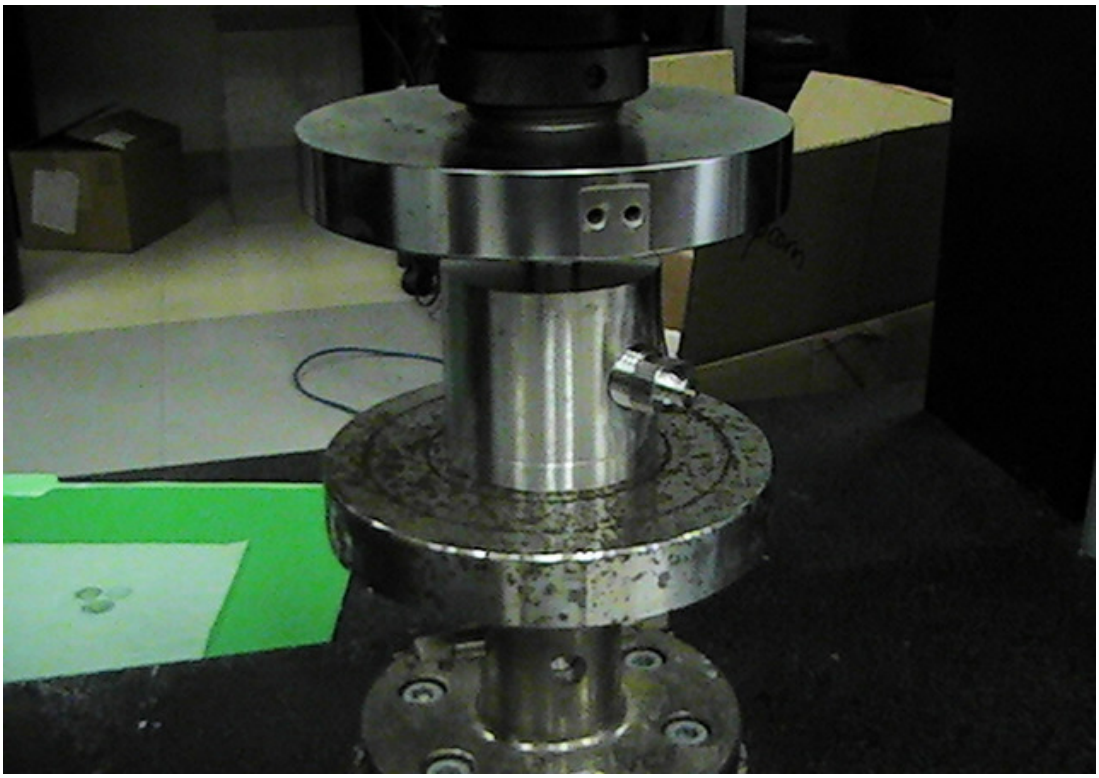

Figure 3.7 – The assembled load cell, positioned in the Instron machine.

Figure 3.8 – The process of collecting drops for measurement, where the refractometer was positioned directly beneath the tap opening.

Graph 3.1 – The shape of a typical graph of load as a function of displacement (isotherm). The region between points A and B is referred to as the infiltration plateau, and between B and C the hydrostatic bulk compression dominates (From [36].)

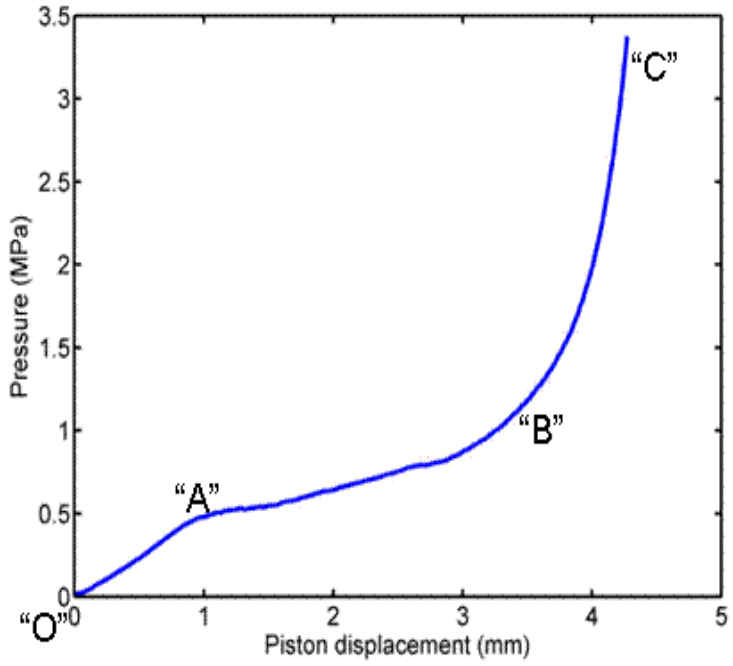

Graph 3.2 – A representative sorption isotherm for the loading of ZSM-5 in NaCl to a maximum of 90 kN (317 MPa). Infiltration of the sample occurred at 22 kN (80 MPa).

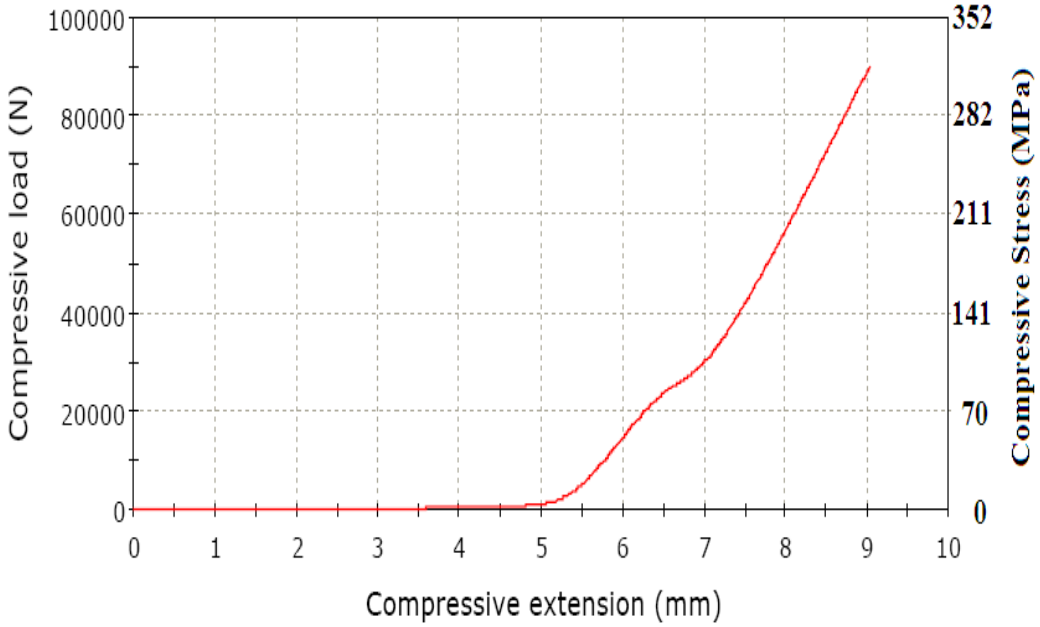

Graph 3.3 – A representative sorption isotherm for the loading of 10-nm, C8-treated HMS to 10 kN (35 MPa). Infiltration of the sample occurred at 5 kN (18 MPa).

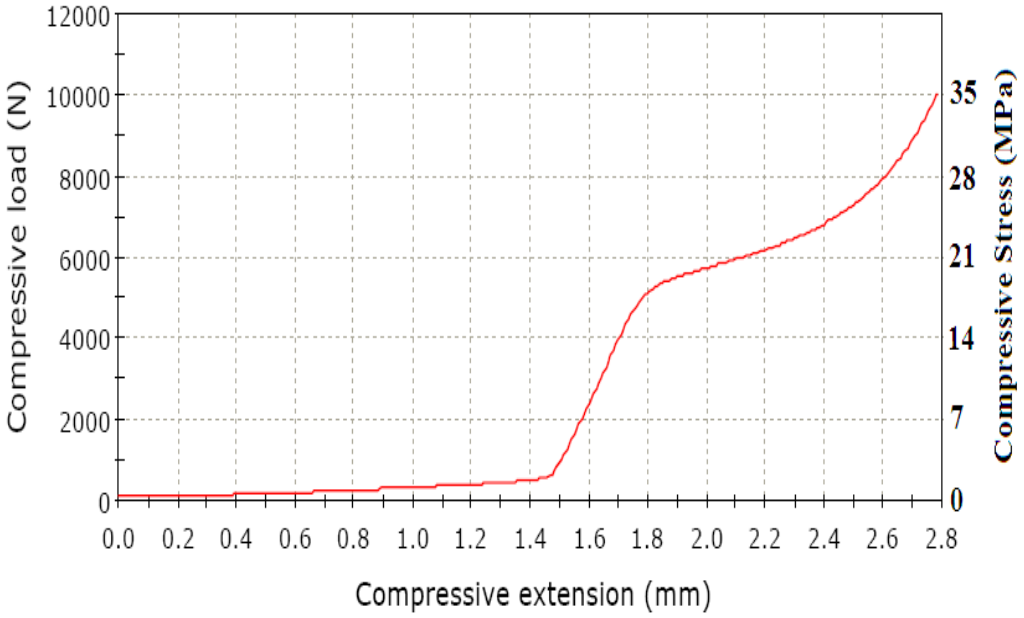

Graph 3.4 – A representative sorption isotherm for the loading of ZSM-5 in LiCl to a maximum of 1 kN (3.5 MPa).

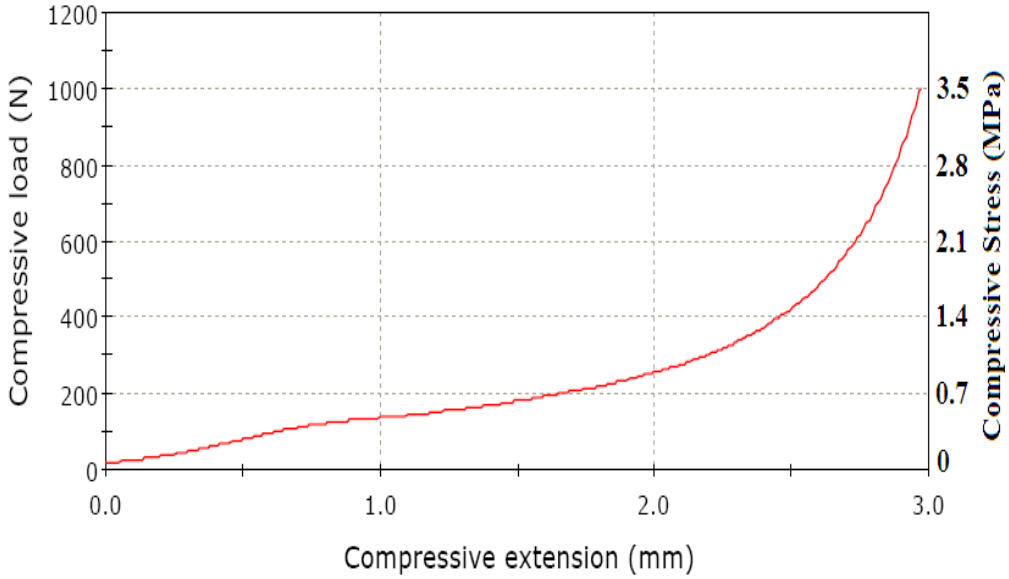

Graph 3.5 – A representative sorption isotherm for the loading of ZY in LiCl to a maximum load of 1 kN (3.5 MPa).

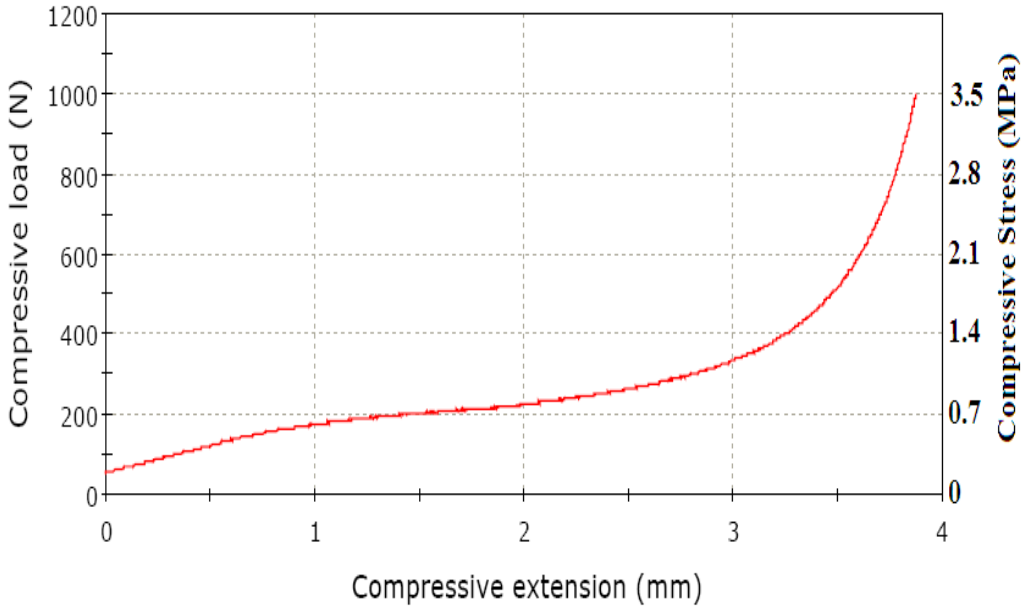

Graph 3.6 – A representative sorption isotherm for the loading of ZY in NaCl to a maximum load of 1 kN (3.5 MPa).

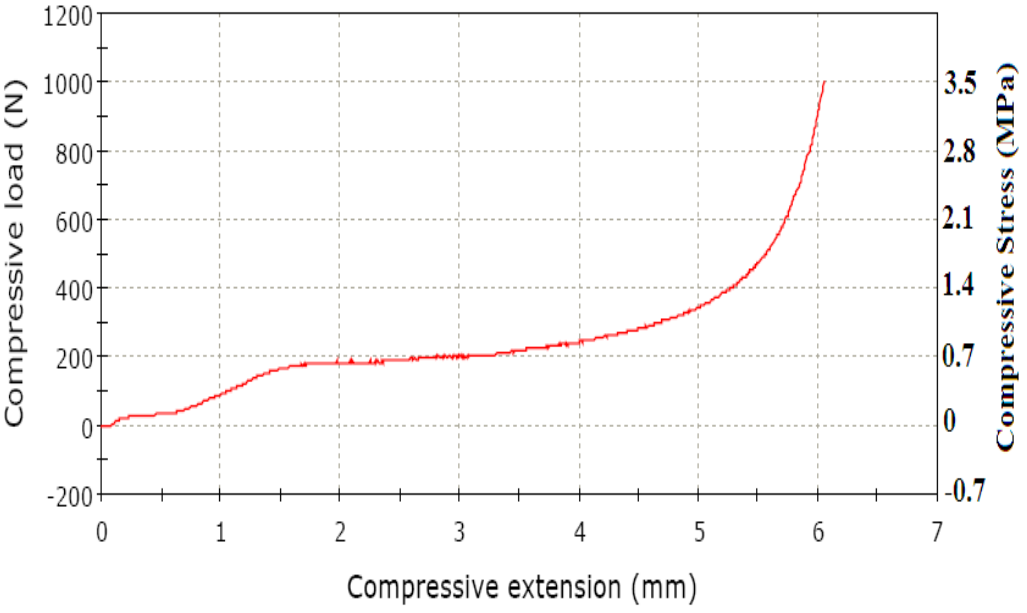

Graph 3.7 – A representative sorption isotherm for the loading of ZY in KCl to a maximum load of 1 kN (3.5 MPa).

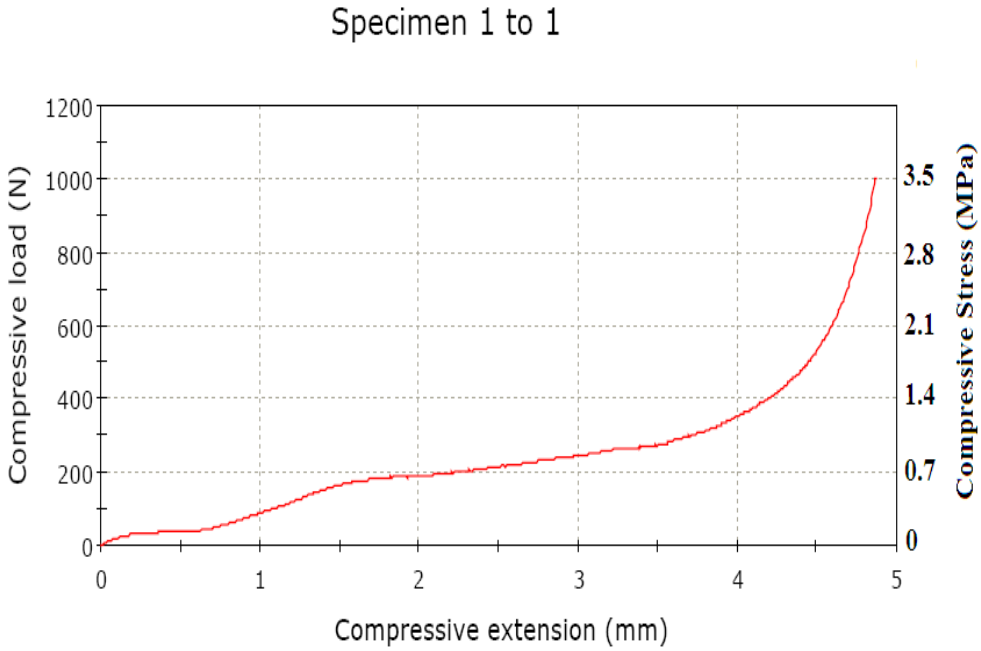

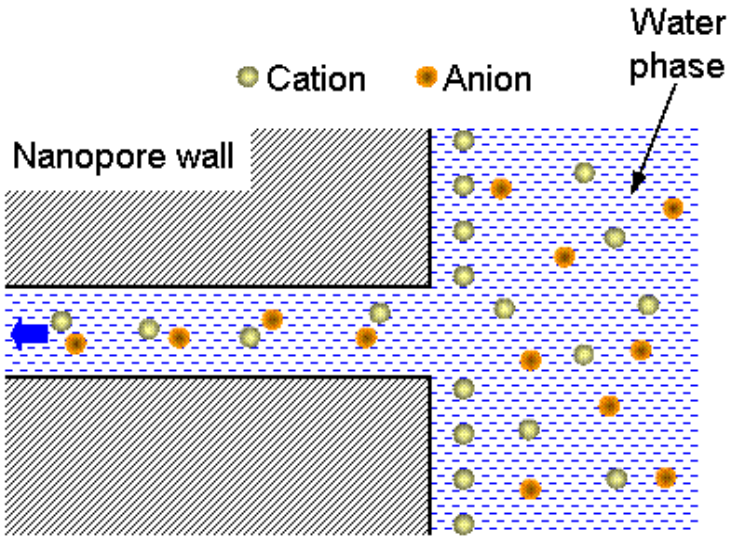

Figure 3.9 – A model of the geometry and molecular behavior at a pore boundary during infiltration. The anions and cations are each arranged in an ion complex (From [36].)

Table 3.2 – Selected values of initial and final concentrations for different concentrations of sodium chloride solution in ZSM-5, loaded to 90 kN.

Initial Concentration (wt%)	Final Concentration (wt%)
3.4%	3.8%
3.4%	4.0%
3.4%	3.8%
3.4%	3.6%
8.2%	8.5%
8.2%	8.8%
8.2%	8.5%
12.4%	13.2%
12.4%	13.0%
12.4%	12.7%
12.4%	13.2%
12.4%	13.1%

Table 3.3 – Selected values for ZSM-5 loaded in different salt solutions.

Salt Type	Load (kN)	Initial Concentration (wt%)	Final Concentration (wt%)
LiCl	1	2.5	2.5
LiCl	1	8.4	8.4
NaCl	1	3.4	3.4
NaCl	1	8.4	8.4
KCl	1	4.3	4.2
KCl	1	8.4	8.4
CsCl	0	9.8	9.8
CsCl	90	9.8	10.7

Table 3.4 – Selected values for ZY loaded in different salt solutions.

Salt Type	Load (kN)	Initial Concentration (wt%)	Final Concentration (wt%)
LiCl	1	2.5	2.7
NaCl	1	3.4	3.6
KCl	1	4.3	4.4
CsCl	0	9.7	10.0
CsCl	1	9.8	10.0
CsCl	0	12.3	12.6
CsCl	1	12.3	12.6

Table 3.5 – Selected values for HMS loadings.

Pore Size (nm)	Salt Type	Load (kN)	Initial Concentration (wt%)	Final Concentration (wt%)
10	NaCl	1	15.0	14.9
6	CsCl	90	9.8	9.8

Graph 3.8 – The percent change in molar concentration as a function of ion size in ZY (From [36].)

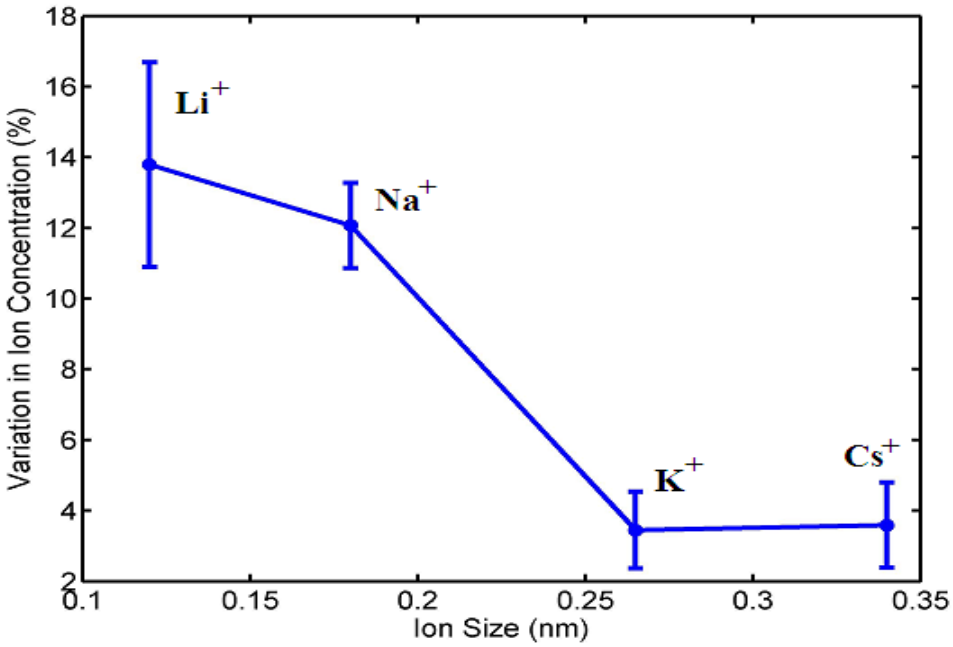

Graph 3.9 – Final molar concentration as function of initial molar concentration for 3.4 wt% NaCl in ZSM-5 subjected to 90 kN of load (From [37].)

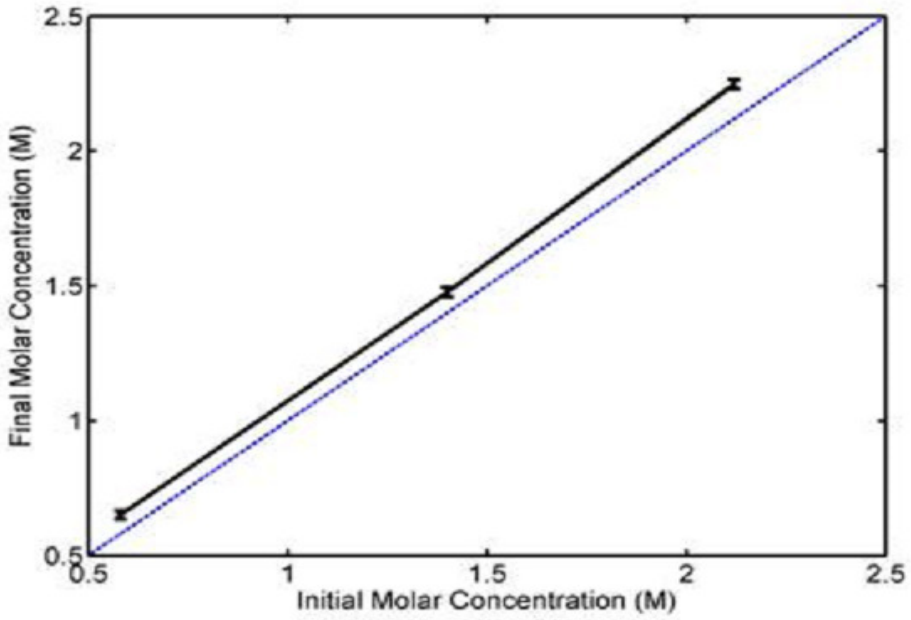

C. Results and Discussion

The testing data showed that for the case of ZSM-5, the salinity increases as long as the hydrostatic fluid pressure exceeds the infiltration pressure (about 80 MPa). The measurements from Table 3.2 were all carried out substantially above this pressure, and thus showed consistent increases in salinity across all ion sizes. For the case of ZY, a smaller pressure was required to achieve ion exclusion. Furthermore, in the case of ZY, there is a dependence of the molar concentration change on the ion size – namely, for larger ions, there is a decrease in the percentage change of solution molarity. In the case of HMS, no significant change in solution concentration was observed over a pore size from 6 to 10 nm.

The results are experimentally significant because all controls indicate that the changes are induced by the internal interaction of the system between the nanoporous powder and the solution. Effects of accidental soluble matter and evaporation were ruled out through the control samples. It was found that the evaporation of a thinly spread drop over the surface of the refractometer leads to a 0.01% increase in salinity per second, which represented an exaggerated condition not encountered during the course of the actual experiments. For realistic settings, the solution is not found to concentrate at all when exposed to the open air for 15 minutes. No change was seen likewise from the mixing of zeolite and solution in a vial. Lastly, no salinity change is seen in pressures below the infiltration plateau as seen on the sorption isotherms.

In general, it can be remarked that the isotherms portray three distinct phases. The first phase is seen as a flat horizontal portion of the curve where air compression occurs. The air does not escape out of the load cell, but rather is forced to dissolve in the solution. The second phase is the infiltration region, where at first the solution is compressed in bulk without entering the pores, but begins to infiltrate where the curve abruptly enters a plateau. The third phase occurs when the graph resumes the bulk compression slope of the early second phase, indicating that the nanopore channels are generally filled. For ZY, there is no easily visible plateau region, since

infiltration occurs continuously up to the tested pressure maximum of 3.5 MPa, where pure bulk compression is slowly approached. For ZSM, the three phases are pronounced, with infiltration occurring at 80 MPa.

The conclusions that can be drawn from the results of the tests on ZY are similar, but a little different from, that which can be drawn from the tests on ZSM-5. In both cases, the surface of the zeolite is hydrophobic before hydrostatically-induced infiltration takes place. Because the pore sizes for both the ZY and ZSM-5 are 0.6 and 0.7 nm, respectively, a classical explanation for the salinity increase is unsatisfactory. Steric mechanisms, on the other hand, may be responsible for the lack of increase in salinity observed for all of the HMS samples, whose pore diameters were an order of magnitude larger than the pore size and begin to approach the Debye length.

As a first-order estimate one may consider the infiltration pressure p_{in} as a function of the interfacial liquid tension $\Delta\gamma$ and effective pore diameter D, as in the Young-Laplace equation [38]

$$p_{in} = \frac{4\Delta\gamma}{D} \tag{3.2}$$

Before infiltration, the interior of the pores is essentially air, or vapor. Given that the air-water interfactial tension is 0.073 N/m, p_{in} is calculated to be 400 MPa for the ZSM-5, which does not agree with experimental data. Clearly, other factors must affect the nature of infiltration. It is also worth noting that while interfacial surface tension is sufficient to explain the increase in infiltration pressure, it is not sufficient alone to explain the difference in the salinity increases of the zeolites, because they are microporous.

Along the pore channels and entrances at the Helmholtz layer, solvated cations can be distorted such that they cause atomic-scale compression on adjacent molecules, described as a “squeezing effect.” This effect must be energetically favorable in the presence of the interactions with the solid substrate. Sufficiently far away from the solid atoms, that is in the Stern layer and beyond, the hydration layers are fully formed.

In the ZY, much lower infiltration pressures were required to observe a salinity increase than ZSM-5. This can due to the inherent crystalline geometries of the ZY pores, which offer a “column resistance” apparently much lower than that of the ZSM-5. Among other factors, the slightly smaller pore size of the ZY, as governed by crystalline geometry, may play into nonlinear effects involving the formation of cation-anion couples. These represent the energetically favorable state in the interior of the nanochannels not otherwise encountered in the bulk solution. If the salinity was measured to be the same or lower in the bulk solution, the concentration of salt solution inside the pores would be greater. Reasonably, this is explained by preservation of the total cation count, as cation exchange cannot occur with zeolite due to electrical neutrality. The testing data was against the assumption that the bulk salinity decreases, so the interior of the pores must have a reduction in salinity instead.

From the experiments involving ZY, 2.27 g of the zeolite must contain about 10.5% of the liquid when fully infiltrated, and 4.6 mL out of 5.2 mL is left standing in bulk. If pure water infiltrated inside the ZY pores, a salinity increase of 11.7% of the bulk should be seen. In fact, this is what was observed for both sodium and lithium cations according to Graph 3.17. Because the KCl and CsCl fall outside of this range, some ions must have infiltrated through the pore opening. However, because a reduction in salinity was observed, the infiltrated solution salinity is reduced. An infiltrated salinity of 70% of the pre-compressed bulk solution best describes the test data for KCl and CsCl. This is also supported by Graph 3.17.

The different responses seen between large and small cations verify the assertion that steric mechanisms are unsatisfactory in capturing the system behavior. It supports the notion of electrostatic interactions governing the filtration of water through the entrance of the pore, consistent with the conclusions supported by Fornasiero’s group. Another explanation may be given by the osmotic pressure, from a stoichiometric perspective. It must be emphasized, again, that the extension of macroscopic osmotic pressure into the nanoscale can provide a zero-order explanation. Assume that the osmotic pressure equals the hydrostatic pressure. For the same stoichiometric ion concentration inside the pore channel, larger cations induce larger osmotic

pressure gradients across the pore entrance solely by virtue of their volumetric occupation. Thus, the water molecules become more volumetrically displaced for larger cations at the same molarity. As a result, fewer large cations are rejected from the interior of the hydrophobic pore channel to require the same change in osmotic pressure than relatively small cations. When combined with electrostatic interactions, the overall behavior is non-linear.

For the ZSM-5 experiments, a similar conclusion is reached for the quantitative estimates regarding the constituents of the pore interiors. In particular, ZSM-5 has a pore volume of 500 mm^3, which leads to 4.6 mL of remaining bulk volume under the peak load. After infiltration, the solution compressed below this value, but does not affect the salinity change. In order to achieve a molar concentration of 0.06 M, the confined liquid essentially consists of pure water.

According to Graph 3.18, there is a slight nonlinearity in the salinity increase. At the lowest concentration of 0.6 M, we observe an increase of 11%. When the sodium chloride concentration is 1.4 M, the molar increase is 5.5%, but at a concentration of 2.1 M, the molar increase is 5.6%. This suggests that, in the post-infiltration stages, pure water enters the pore at sufficiently low bulk concentrations, and this ion exclusion is robust up to a critical concentration. There may be slight presence of sodium cations inside the pores past the critical concentration. Since sodium cations are considerably smaller than the pore diameter, steric exclusion may be influential in the upper tail of the pore size distribution. However, this conclusion is open for further investigation. What remains known is that the electrostatic interactions, and possibly osmotic pressures, remain dominant as in the case for ZY. This is evident from the fact that nearly pure water infiltrates the pores over a wide range of pressures, for the sodium chloride solution.

As the maximum pressures were reached for ZSM-5 were only 3.5 MPa outside of the sodium chloride bin, there is a lack of infiltration and consistently no salinity increase in the bulk solution. An exception is the case of cesium chloride, which was tested beyond 80 MPa and observed to have an increase of about 10% in molarity. The consistency of the molarity increase in cesium chloride is inconsistent with that of the ZY via the osmotic mechanism by itself, suggesting that other factors governing ion exchange may come into play, such as the

electrostatic interactions at the pore openings. One possibility involves the zeta potential, which arises from the natural polarization of the Helmholtz layer. The effect of the zeta potential is not evident for larger pores, but becomes so on the nm scale. At such scales, the pore entrance is dominated by the electric field. Like-charged anions will be repelled by the zeta potential across the pore interface, but cations will be facilitated. Because the pore interior tends to be electrically neutral, the cation uptake is quickly suppressed. Ion concentrations, themselves linear, may have a nonlinear effect on the zeta potential (*viz*., concave down), which may account for the presence of a critical concentration in ZSM-5. The absence of a strong zeta potential in ZY can be a result of their different cation compositions in the crystal structure, or the strength of the osmotic mechanism relative to that of the electrostatic one.

It is also worthwhile to note that simulation indicates that simulation studies have found a water molecule configuration that is akin to a double-helical structure [38]. This is akin to structural buckling of long circular columns in full elastic spaces [39]. The implications for this may have a bearing on the dynamics of water absorption and ion exclusion in the future.

D. Conclusion and Prospectus

It is seen that a variety of factors including osmotic pressures and electrostatic interactions are suspected of affecting the ion exclusion in zeolites. If carefully extended into the nanoenvironment of a zeolite pore, osmosis can be speculated to partially explain the nonlinear uptake in different sizes of cations for a ZY. Electrostatic interaction, such as the zeta potential, can explain the presence of a strong screening effect across the interface of a pore entrance in ZSM-5. In both cases, interfacial surface tension plays a role in determining the infiltration pressure, but not how cations enter into the pores.

The conclusions drawn from this work figure relevantly into the applications of water isolation, for the very opposite reason why the salinity increases are encountered in the experiments: zeolites do have the ability to separate water molecules from cations and anions, although the mechanisms remain complex. Because the hydrophobic pores contain pure water at and above the infiltration pressure for sodium chloride, one can design a pressure-induced filtration system out of this using a membrane configuration. Zeolite membranes' synthesis and roles are an active research topic, but the current overall applicable interest appears to be on gas segregation [40, 41, 42, 43]. Because ZY and ZSM-5 are both cost-efficient materials, they may be favorably developed in practice.

The main challenge in developing a filter configuration is the large pressures needed for ZSM-5. If that material is no longer considered, one is left with ZY. One can infer from the experiments that on a timescale of minutes, one mL of water may infiltrate into the pores. The effect of different loading rates should be established, and after that, the surface area of membrane topology needs to be successfully convoluted in order to facilitate rapid filtration of seawater, because 2.27 g of zeolite in the powder form translates to at least 1600 m^2 worth of membrane area, so this is a daunting task to accomplish.

The HMS samples showed little to no ion exclusion effects. However, this does not rule out their potential use as water filters, because the effect of the zeta potential (electrical effects)

across those sizes remains unknown for different surface treatments. If an HMS can be successfully treated so as to produce considerable electrostatic screening effects, water filtration may be.

IV. EXPERIMENT: CARBON ELECTRODES IMMERSED IN SALINE SOLUTIONS

A. Motivation and Background

One of the novel ways to extract pure water from seawater is through the electrosorption technique. The research and development of nanoporous materials makes this possible, for the advantage of their extremely high surface area to volume ratio. If macroscopic materials are used, on the other hand, it is simply impossible. Consider two flat electrode foils made of graphite, each measuring 1 m^2 and weighing 0.5 grams. Sandwiched in between is a 1-mm thick layer of seawater (sodium chloride concentration of 3.2 wt%) between them. The volume of water that can be purified is expressed as

$$m = \frac{sA}{MN_A e} \tag{4.1}$$

Where m is the volume of water purified in L, s is the surface ion density, A is the specific surface area of the electrode, M is the molar concentration of ions, and the product $N_A e$ - between Avogadro's number and the elementary charge - is Faradays constant, 96,485.34 C/mol. In the example, M is equal to the salinity of seawater, 0.545 M. If the charge density s is taken as 0.015 C/m^2 for graphite, then m is 2.9 E-7 liters for that single gram of electrode, which is impossible. Even with conventional technologies, the manufacture of a 1 m^2 graphite electrode weighing 1 gram is already difficult. Thus, one can easily see why it is difficult to produce realistic electrosorption-based desalination systems.

With nanoporous materials, the specific surface area is increased by anywhere between two to four orders of magnitude. The extremely high specific surface areas also mean that virtually none of the volume of the material itself is shielded from chemical corrosion. Therefore,

only the most inert solids can be used for suitable nanoporous electrodes. There are three possibilities: gold, platinum, and carbon. The first two are too expensive from an economical standpoint, and are obviously abandoned in favor of carbon. Moreover, nanoporous carbons have much larger surface areas. The forms of carbon discussed earlier include CNTs, carbon black, and carbon aerogels. Because of the intense interest in CNTs, we redirect our attention to the other two, which also happen to be more economical as well.

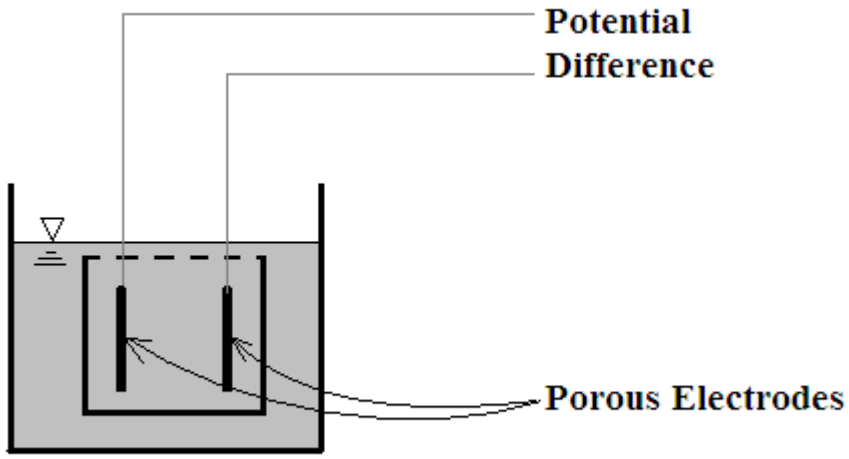

Figure 4.1 – A schematic of the concept of electrosorption. The inner chamber can be separated from the main tank.

A design paradigm of a practical carbon-based electrosorption system is illustrated in Figure 4.1. First, mechanically filtered seawater fills a tank that contains two electrodes. The electrodes themselves are situated in an almost isolated chamber, except the top allows water to enter inside. Once the electrodes have saturated, the apparatus can be lifted out, and the rest of the solution is considered the filtrate. The size proportion of the tank and the chamber can be adjusted; it is ideal for the inner chamber to be very small relative to the tank volume. In the case where ion adsorption is imperfect or incomplete in one process, there can be more than one iteration whereby the filtrate from one process is considered the entry solution in the next iteration, and so on.

B. Experimental

Nanoporous carbon in the form of carbon black was used (Cabot BP2000). It was prepared by drying at 120 degrees Celsius and analyzed with a porosity analyzer (Micromeritics Tristar 3000). The specific surface area was found to be 1260 m^2/g, the pore diameter 17 nm, and the pore volume 2.2 cm^3/g. Mixed with the carbon black were PVDF (Aldrich) and acetylene black (Soltex AB50) in the ratio of 8:1:1 by weight, respectively. The powders were mixed in an agate mortar and pestle. When uniformity was achieved, the mixture was compressed at 260 MPa. The compression was done with a load cell whereby a copper sleeve was used to confine the powder mixture. The carbon black discs taken out each weighed about 1 gram.

The carbon discs (Figure 4.7) were assembled as part of an electrode module (Figures 4.5, 4.8, 4.9), in order to simulate an environment with high bulk electrode occupation and low solution volumes. The module consisted of two carbon discs separated by a porous filter. An epoxy mold was set up which featured a semicircular indentation with a volume of 0.8 mL. The discs were then placed inside the semicircular epoxy mold. Filter paper was used as a separator between the carbon disks. Two metal plates are used as charge collectors. The two plates are separated by three films of polypropylene, all of matching dimensions, in an alternating fashion in lieu with the carbon discs. The middle film had a semicircular cut-out on the bottom edge. The metal plates were secured to one side with a clamp such that there is a semicircular protrusion of the pair of carbon disks outside the bottom edge of the metal plates. The protrusion is suspended several millimeters above the bottom of the indentation in the epoxy mold (in order to avoid breakage), and clamped in place.

Charge measurement from a nanoporous carbon required three main components, as seen in the circuit diagram in Figure 4.6. The first component was a DC Power Source (Protek 6003B) which supplies an electrical potential difference. Terminals were connected to alligator clips, with the negative terminal grounded. A 10–Ohm resistor was set up in parallel with a DAQ which detects discharge electrical current. In general, the setup portrayed by Figure 4.6 is similar

to manual measurement of a capacitor with a long time constant and low rates of self-discharge. The “system” in Figure 4.6 is therefore denoted by a capacitor in the circuit diagram. The function of the DAQ for reading current is similar to that of an operational amplifier, in which it draws little current by itself to make a measurement.

Once the DC power source was connected to both plates, the current was verified as reading zero to ascertain the absence of shorting. Using 1.0 V potential difference on the power supply, a salt solution filled the epoxy mold. The salt solution was dilute aqueous sodium chloride, in different concentrations. The presence of current on the DC power source was verified. After three minutes of current decay, the leads to the DAQ, were connected to the metal plates, effectively closing the switch in Figure 4.6. The power source is quickly turned off. The decay is observed.

The total charge that is stored on a capacitor can by derived by integrating the current over time, using Ohm’s law:

$$Q = \int I \, dt = \int \frac{V}{R} \, dt \tag{4.2}$$

Salinity changes were tested for, by pipette transfer of two drops of the electrolyte onto a refractometer before the discharge.

Figure 4.2 – The three ingredients used to produce the electrode, from left to right: PVDF, AB50, and BP2000. The agate mortar and pestle is shown on the bottom.

Figure 4.3 – A piston typical of the type used to compress the mixture. Omitted from the picture is a copper sleeve which is inserted around the perimeter to reduce mechanical friction.

Graph 4.1 – The adsorption-desorption isotherm curves obtained for BP2000, on linear abscissa. The high rate of increase towards the end indicates that the average pore size is mesoporous.

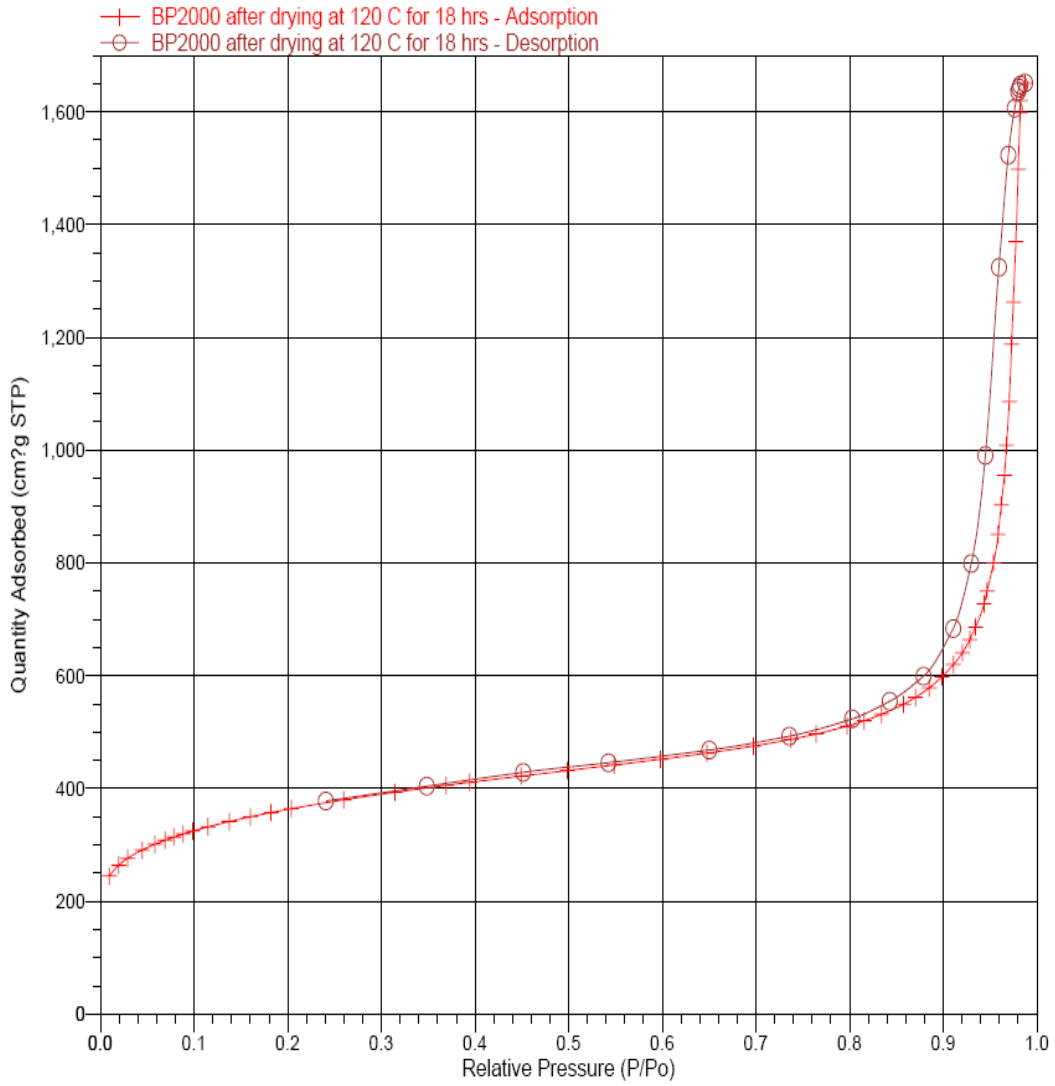

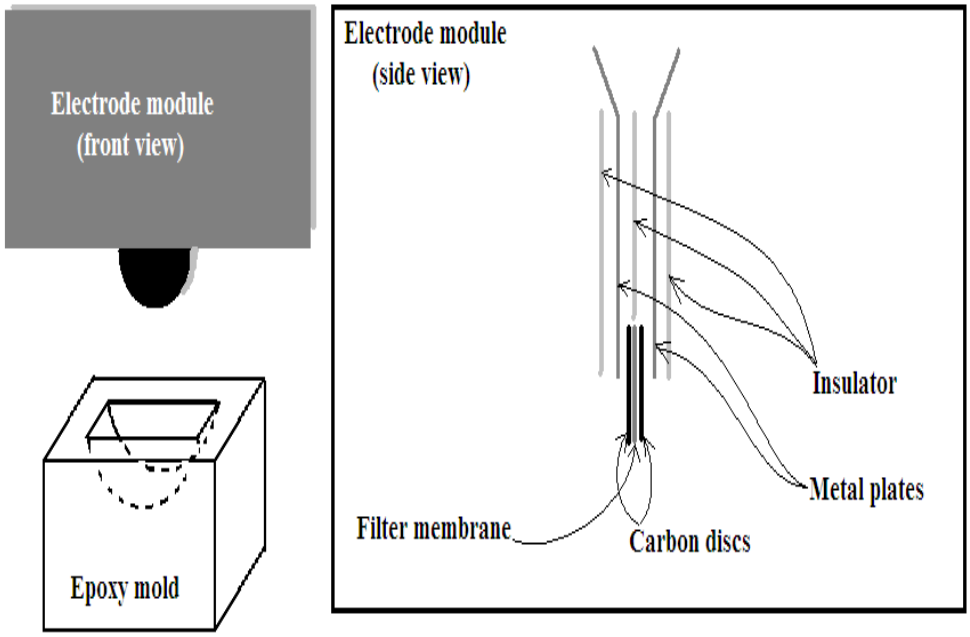

Figure 4.4 – A schematic of the electrode module and the epoxy mold. The epoxy mold holds the solution. The inset shows a cross of the electrode module when fully assembled, through the front view midpoint.

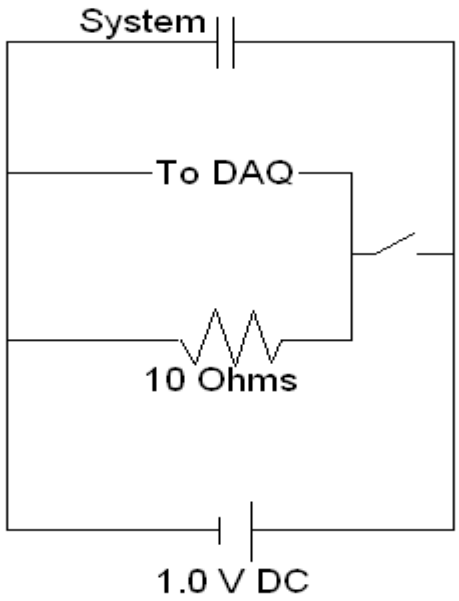

Figure 4.5 – The entire system circuit schematic. Note the “system” is the electrode module with the carbon discs inserted into the electrolyte solution.

Figure 4.6 – A picture of the carbon disks (three in the upper right), with a penny for scale.

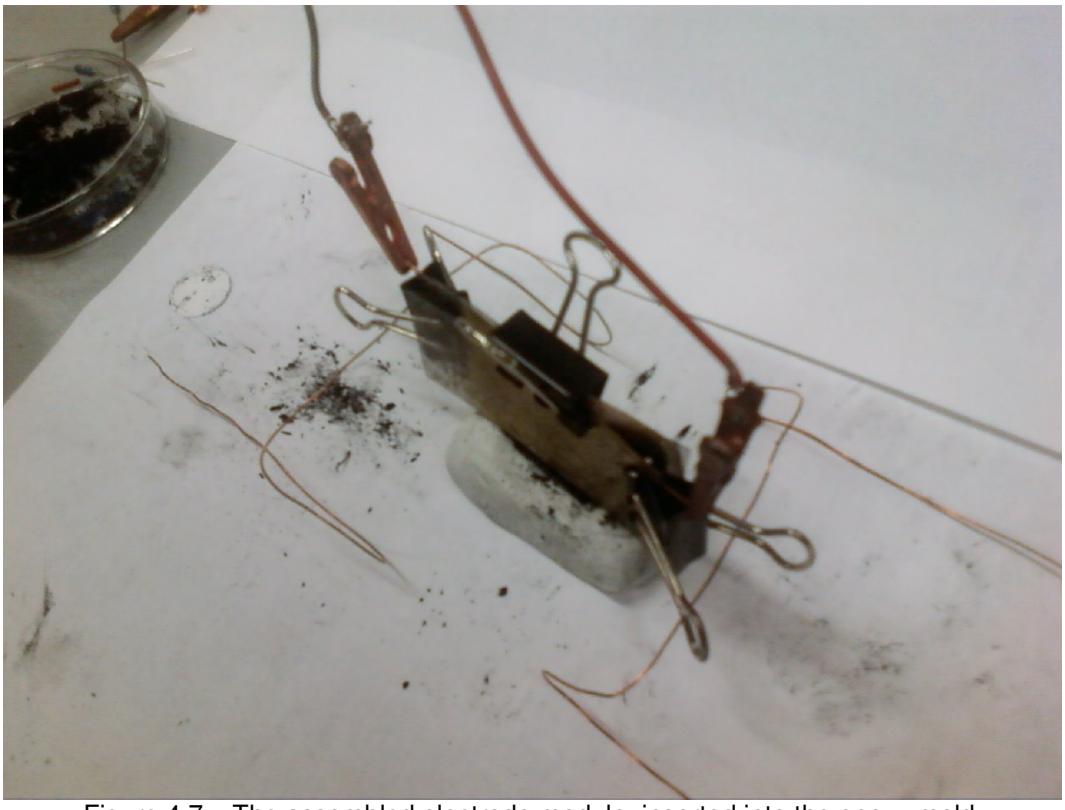

Figure 4.7 – The assembled electrode module, inserted into the epoxy mold.

Figure 4.8 – The electrode module with the epoxy mold filled with solution. Copper leads were used to connect the metal plates to the alligator clips.

Graph 4.2 – Voltage as a function of time for a 1.6 wt% NaCl solution using Au plates, and charged to 1 volt for 5 minutes. The switch was closed first, as visible in the brief plateau, and the power was turned off as indicated by the voltage drop. The measurement duration was 40 seconds.

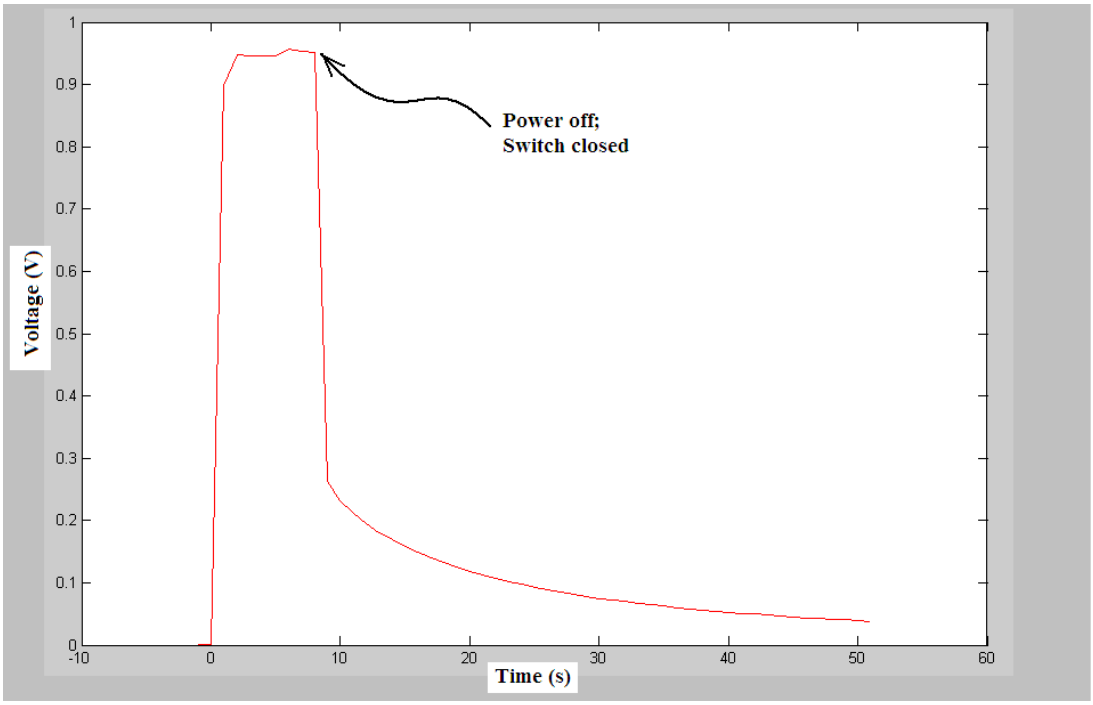

Graph 4.3 – Voltage as a function of time for a 3.4 wt% NaCl solution using Au plates, and charged to 1 volt for 5 minutes. The switch was closed first, as visible in the brief plateu, and then the power was turned off as indicated by the voltage drop occurred. The time constant was longer for this case, so the measurement duration was 300 seconds.

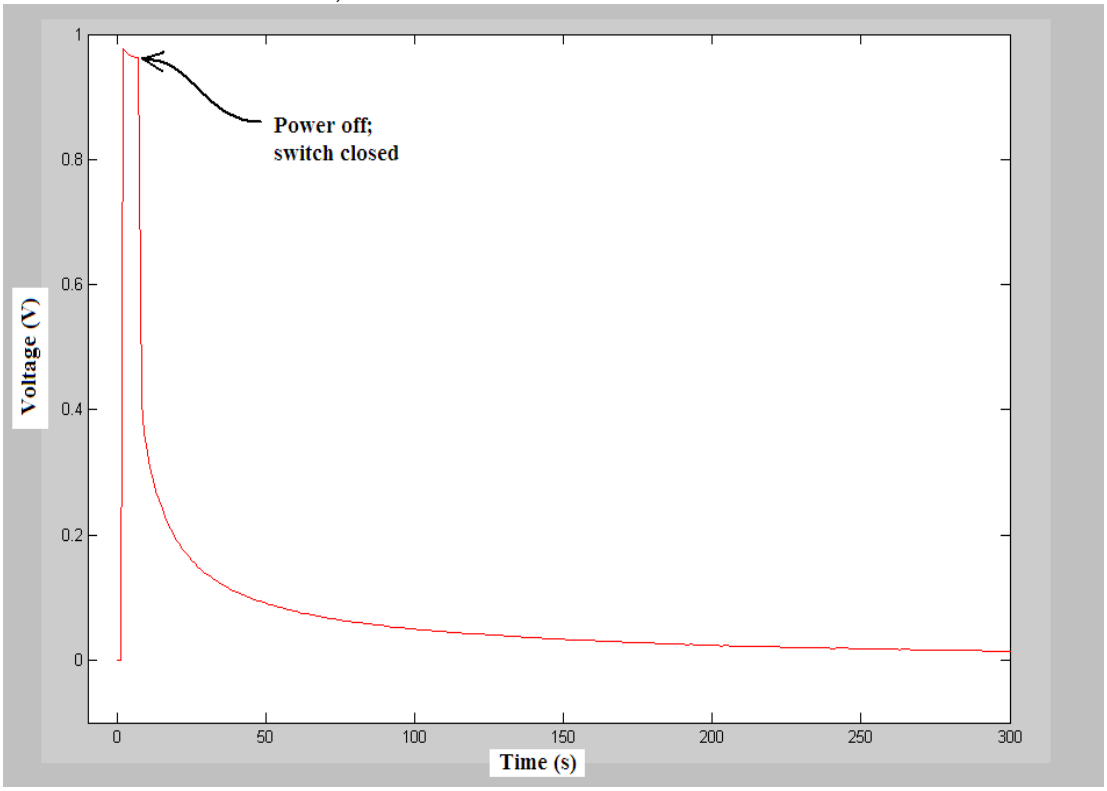

Table 4.1 – A table of characteristics of trials of different NaCl concentrations charged to 1 V, then discharged. The onset voltage was the first reasonably measureable ordinate in the graphs. The time constant is defined as the time it takes for 63% of the current to decay.

Solute Concentration	Plate Material	Onset Voltage	Average Discharge	Avg. Time Constant
3.4 wt% NaCl	Au	0.5 V	0.83 C	26 s
1.6 wt% NaCl	Au	0.26 V	0.66 C	15 s
0.8 wt% NaCl	Au	0.1 V	N/A	N/A
3.4 wt% NaCl	Al	0.0 V	N/A	N/A
3.4 wt% NaCl	302 SS	0.1 V	N/A	N/A

C. Results and Discussion

Estimating the charges from Figs. 4.2 – 4.3, one can estimate the charges of the carbon discs in accordance with Table 4.1. It is found that higher concentrations of electrolytes have a nonlinear (less efficient) storage of charge in relation to the increase in salinity. The time constant is greater for higher concentrations in a likewise fashion.

The findings are significant because none of the voltages exceeded the breakdown (electrolytic) voltages. In general, the breakdown voltage is highly dependence on both the electrode and solution makeup. It was generally seen, however, that for the salt solutions tested, the breakdown voltage varied between 1.3 V and 2.6 V using graphite electrodes.

The time constants seen in Table 4.1 may be explained by the diffusion process. Recall earlier discussions of the double layer; near the solid surface, the solvated ions represent a locally saturated state. The bulk saturation point of NaCl at STP is about 40 wt% essentially representing a constant, but the comparison is not exact because of the “squeezing effect,” also discussed earlier. Because the adsorption layer contains an essentially saturated solution, it is at an essentially constant value. Consequently, once the electric field ceases, less time is required for molecular diffusion across a smaller salinity gradient in dilute solutions, and vice versa.

There is considerable attention paid to adsorption layer phenomena in the presence of electric fields. With no electric field, ions build up across the double layer and governed by phenomena related to solid surface interactions, such as the Van der Waals interaction. When an electric field is present, however, the adsorbed layer grows in thickness. One possible explanation for this is that the surface potentials “assimilate” the saturated ion layers into the solid surface [44]. The dimensions of the adsorbed layer are estimated to be somewhere in the range of 70 nm to 100 nm, but this could vary between different materials [45]. The investigations about the exact nature of this are still ongoing. Inside the electrodes, the electron excess and deficit is manifested in the ion buildup of the adsorbed layer. Indeed, the apparent growth of the adsorbed layer is responsible for the observed capacitance of the BP2000.

The liquid was measured by a refractometer on multiple trials. However, no change in salinity was observed. In order to quantitatively understand this result, we calculate the amount of ions present in a typical experimental solution, and equate it as the number of elementary charges present. In 0.8 mL of 1.6 wt% NaCl, the number of ions is calculated to be 3.0E20 ions, or about 150 C of charge. Compared to 0.7 C, a refractometer would need to detect about 0.5% difference in the salinity of the solution, or a 0.02 wt% in difference. This is not possible with the refractometer utilized, given its accuracy of 0.2 wt%. Furthermore, any significant changes detected on the hundredths-of-percent level are highly suspect to confounding by evaporation. In spite of this, an order-of-magnitude analysis of Equation 4.1 reveals that 0.1 mL of pure water should be detectable – in the preceding example, 0.2% should be the theoretical maximum.

Further improvements can also be made to the actual makeup of the carbon discs. After wetting, the consistency of the electrode resembled that of dough-like material. This could result in the loss of electrical conductivity throughout the surfaces of the electrode, or at least a loss in electrical field strength. It is proposed that mechanical compression of BP2000 to greater pressures can preserve (or even increase) its surface area, while at the same time reducing the pore volume. From previous experiences, it has been suggested that this is not the case.

To further investigate if a difference in the case of a structurally intact porous carbon, another trial was performed with carbon aerogel and a dilute solution of lithium chloride. No changes in salinity were detected, against expectations.

Further experimentation on this matter is warranted before definitive conclusions can be drawn about the practical efficacy of electrosorption by carbon aerogel or carbon discs.

D. Conclusion and Prospectus

The current findings indicate that adsorption of ions, while still too small to detect, occur in amounts just one order of magnitude less than that which may be detected using the refractometer.

Because seawater salinity and electrolytic breakdown are difficult factors to change, the materials used for the porous electrodes are the sole route for improvement in the electrosorption systems. There are a variety of strategies to pursue. For example, pore volume can be reduced through chemical precipitation means. The reduction of pore volume means that less solution is absorbed in the interstitial spaces, leading to greater bulk volumes of solution for utility. Another strategy is to increase specific surface area. Although difficult, it is not impossible. The temperature used to create BP2000 is similar to the flame temperature of combustion. Exposure of carbon black to temperatures, such as that of plasma environments for CNT creation, is worthy of interest.

Whatever the strategies used for the improvement of nanoporous carbon electrodes may be, it is certain that whenever the one order-of-magnitude gap is closed, practical applications are already possible. This is due to the iteration scheme mentioned previously, and the low amounts of power required for generating 1 V of potential difference combined with the mechanical transport of water, is still trivial compared with the relatively sophisticated systems for conventional filtering by reverse osmosis.

V. SUMMARY

Nanoporous materials are of key engineering interest, because they are versatile in many ways. We have outlined the basic key defining characteristics, types, methods of fabrication, and methods of surface treatment for nanoporous materials. A key interest is the extraction of usable water from natural environments - specifically, the air and the ocean. Several ways to isolate pure water have been explored in the three experiments.

Atmospheric condensation is a phenomenon that can be exploited by nanoporous materials, due to their advantageous compact surface areas. The surfaces of a very large condenser occupying the volume of a large warehouse can be literally held in the palm of the hand. The drawback with compacting to this degree is that a limited amount of air can be present inside the material at a given time. Yet, other routes to exploit high surface areas, such as increasing the size of nanoporous sample and hydrophobic surface treating, should be able to result in practical systems. From the observed results, there is slight hint of significant findings, but faces confounding variables such as pressure drop due to fluid flow, the tendency of porous materials themselves to insulate when place in an artificially refrigerated setting, and the unresolved issue of condensation in relation to evaporation and diffusion, and controls against a hydrophilic-treated surface. A potentially powerful way of improving the system performance is to treat a material which may be electrically activated to be hydrophobic and hydrophilic.

Desalination of seawater is possible by two routes: mechanical filtration and electrosorption.

The first route was investigated using zeolite. The experiments found that zeolite does have a significant effect on the absorption of cations and anions, and suggested pure water infiltration in the pores for select cases. A variety of known and speculative mechanisms is proposed to account for the observed ion segregation.

The second route was investigated using carbon black electrodes. The usefulness of this method is due to the low energy-intensive nature compared to mechanical methods. Only

one volt is required for electrosorption, and the maximum voltage is inherently limited by the breakdown voltage between the electrode and the solution. It was found that while there was no significant difference in the salinity measured after the solution was fully polarized, measurement is possible after a ten-fold increase in surface area or ten-fold decrease in the pore volume.

VI. REFERENCES

1. Buzea, C., Pacheco, I. I., and Robbie, K. *Biointerphases*, **2**, *4* (2007), pp. MR17–MR71.

2. Lu, A.-H., and Schüth, F. *Adv. Mater.*, *18* (2006), p. 1798.

3. Schmidt, I., Boisen, A., Gustavsson, E., Ståhl, K., Pehrson, S., Dahl, S., Carlsson, A., and Jacobsen, A. J. H. *Chem. Mater.*, *13* (2001), p. 4416.

4. Rytwo, Giora. *Rev. Soc. Esp. Mineralogía*, **9** (2008), pp. 15 – 17.

5. Skandan, G., and Singhal, A. *Perspectives on the Science and Technology of Nanoparticle Synthesis*. In: Nanomaterials Handbook (Gogotsi, Y., ed). CRC Press, Boca Raton, Florida (2006).

6. Feldman, M., and Desrochers, P. *Industry and Innovation*, **10**, *1* (2003).

7. Scott, Raymond P. W. Silica Gel and Bonded Phases: Their Production, Properties, and Use in LC. John Wiley & Sons Ltd., Chichester, West Sussex, England (1993).

8. Brunauer, S., Emmett, P. H., and Teller, E. *J. Am. Chem. Soc.*, **60** (1938), pp. 309 – 319.

9. Langmuir, Irving. *J. Am. Chem. Soc.*, **38** (1916), pp. 2291 – 2295.

10. Grillet, Y., and Llewellyn, P. L. *Adsorption Properties of the Silica Surface*. In: The Surface Properties of Silicas (Legrand, A. P., ed). John Wiley & Sons Ltd, Chichester, West Sussex, England (1998).

11. White, Frank M. Fluid Mechanics (6^{th} ed). McGraw-Hill, New York, New York (2008).

12. Qiao, Y., Punyamurtula, V. K., Han, A., and Lim, H. *J. Power Sources*, **183** (2008), pp. 403 – 405.

13. Fornasiero, F., Park, H. G., Holt, J. K., Stadermann, M., Grigoropoulos, C. P., Noy, A., and Bakajin, O. *PNAS*, **105**, *45* (2008), pp. 17250 – 17255.

14. Harris, Peter J. F. Carbon Nanotube Science: Synthesis, Properties, and Applications. Cambridge University Press, Cambridge, UK (2009).

15. Yumura, Motoo. *Synthesis and Purification of Multi-Walled and Single-Walled Carbon Nanotubes*. In: The Science and Technology of Carbon (Tanaka, K., Yamabe, T., and Fukui, K., eds). Elsevier Science Ltd., Oxford, UK (1999).

16. Donnet, J.-B., and Voet, A. Carbon Black: Physics, Chemistry, and Elastomer Reinforcement. Marcel Dekker, Inc., New York, New York (1976).

17. Kuhner, G., and Voll, M. *Manufacture of Carbon Black*. In: Carbon Black: Science and Technology, 2^{nd} ed (Donnet, J.-B., Bansal, R. C., and Wang, M. J., eds). Marcel Dekker, Inc. New York, New York (1993).

18. Richner, R. Müller, S., Kötz, R., and Wokaun, A. *Studies of Activated Carbon and*

Carbon Black for Supercapacitor Applications. Electrochemistry Laboratory, Paul Scherrer Institute. http://ecl.web.psi.ch/Publications/cap_pub/ Roy.pdf

19. Heckman, F. A., and Harling, D. E. *Rubber Chem. Tech.*, **39** (1966), p. 1.

20. Zhao, D., Feng, J., Huo, Q., Melosh, N., Fredrickson, G. H., Chmelka, B. F., and Stucky, G. D. *Science*., **279** (1998), pp. 548 – 552.

21. Pekala, R. W. and Alviso, C. T. *Carbon Aerogels and Xerogels*. In: Novel Forms of Carbon (Renschler, C. L., Pouch, J. J., and Cox, D. M., eds). Materials Research Society (1992).

22. Chen, L., Zhu, G., Zhang, D., Zhao, H., Guo, M., Shi, W., and Qiu, S. *J. Mat. Chem.*, **19** (2009), p. 2014.

23. Kim, Taewan., "Synthetic Methods for Macroporous Glass by Phase Separation." Research Report, University of California, San Diego (2009).

24. Li, X., Cao, Z., Liu F., Zhang, Z., and Dang, H. *Chem. Lett.*, **35**, *1* (2006), pp. 94 – 95.

25. Sarawade, P. B., Kim, J.-K., Hilonga, A., and Kim, H. T. *J. Haz. Mat.*, **176** (2010), pp. 576 – 580.

26. Rollman, L. D., Valyocsik, E. W., and Shannon, R. D. *Inorg. Synth.*, **22** (1983), pp. 61 – 68.

27. Attard, G. S., Glyde, J. C., and Göltner, C. G. *Nature*, **378** (1995), pp. 366 – 367.

28. Rollman, Louis D. *Synthesis of Zeolites, An Overview*. In: Zeolites: Science and Technology (Riberiero, F. R., ed). Martinus Nijhoff Publishers, The Hague, The Netherlands (1984).

29. Jacobs, P. A., and Martens, J. A. Synthesis of High-Silica Aluminosilicate Zeolites. Elsevier Science Publishers B.V. (1987), p. 53.

30. Yang, D.-Q., Rochette, J.-F., and Sacher, E. *Langmuir*, *21* (2005), p. 8543.

31. Heijman, S. G. J., and Hopman, R. *Colloids and Surfaces A: Physiochem. Eng. Aspects*, *151* (1999), pp. 303 – 310.

32. Hanafi, A., and Abdel-Latif, M. A. *J. Eng. App. Sci.*, **56**, *3*, pp. 269 – 282.

33. Li, Z., and Zhang, Y. *Study of the electro-sorption desalination by carbon aerogel electrodes*. ICCBE 2009, 4 pp.

34. Muller, R. A., and Oberlander, T. M. Physical Geography Today: A Portrait of a Planet (2^{nd} ed). Random House, Inc. (1978), pp. 91 – 94.

35. Incropera, F. P., Dewitt, D. P., Bergman, T. L., and Lavine, A. S. Introduction to Heat Transfer (5^{th} ed). John Wiley & Sons (2007), pp. 136, 878.

36. Chow, B. J., Lu, W., Lim, H., Han, A., Chen, X., and Qiao, Y. *Effective Surface Ion Density in a Zeolite Y* (in draft).

37. Chow, B. J., Lu, W., Lim, H., Chen, X., and Qiao, Y. *Ion-Repelling Effect of Nanopores in a Zeolite* (in draft).

38. Qiao, Y., Liu, L., and Chen, X. *Nano Lett*, **9**, *3* (2009), pp. 984 – 988.

39. Svenšek, D., and Podgornik, R. *Phys. Rev. E*, **77**, 031808 (2008).

40. Chen, Y., Zhu, G., Peng, Y., Yao, X., and Qiu, S. *Micro. Meso. Mat.*, **124** (2009), pp. 8 – 14.

41. Bowen, T. C., Noble, R. D., and Falconer, J. L. *J. Membrane Sci.*, **245** (2004), pp. 1 – 33.

42. Sano, T., Kiyozumi, Y., Kawamura, M., Mizukami, F., Takaya, H., Mouri, T., Inaoka, W., Toida, Y., Watanabe, M., and Toyoda, K. *Zeolites*, **11** (1991), pp. 842 – 845.

43. Kusakabe, K., Yoneshige, S., Murata, A., and Morooka, S. *J. Membrane Sci.*, **116** (1996), pp. 39 – 46.

44. Kovalenko, Andriy. *J. Comp. Theo. Nanosci.*, **1**, *4* (2004), pp. 398 – 411.

45. Kampf, N., Ben-Yaakov, D., Andelman, D., Safran, S. A., and Klein, J. *Phys. Rev. Lett.*, **103**, 118304 (2009).